Energy Advances

ROYAL SOCIETY OF CHEMISTRY

PAPER

View Article Online
View Journal | View Issue

Cite this: *Energy Adv.*, 2025, 4, 1279

Impact of crystal structure on the thermoelectric properties of n-type $SrTiO_3$

Alveena Z. Khan, Joseph M. Flitcroft and Jonathan M. Skelton *

We present a detailed first-principles study of the electrical and thermal transport, and the thermoelectric figure of merit *zT*, of the oxide perovskite $SrTiO_3$ in the orthorhombic *Pnma*, tetragonal *I*4/*mcm* and cubic *Pm*$\bar{3}$*m* phases. Analysis of the lattice thermal conductivity shows that the "particle-like" contribution, κ_p, is highest in the *Pm*$\bar{3}$*m* phase due to larger phonon group velocities. We also find that all three phases show significant heat transport through glass-like interband tunnelling. On the other hand, we predict the cubic and orthorhombic phases to show superior n-type conductivity, due to significantly stronger polar-optic phonon scattering and shorter electron lifetimes in the tetragonal phase. Due to its superior electrical properties, we predict that the *Pm*$\bar{3}$*m* phase will attain a 25% larger high-temperature *zT* than the *I*4/*mcm* phase, while we predict the best *zT* can be obtained for the *Pnma* phase due to its favourable electrical properties and low κ_{latt}. This work provides new insight into the impact of structure type on the thermoelectric performance of oxide perovskites, and indicates targeting particular structure types, *e.g.* through chemical doping, could provide a facile route to optimising the *zT* of $SrTiO_3$ and related systems.

Received 16th April 2025,
Accepted 18th August 2025

DOI: 10.1039/d5ya00105f

rsc.li/energy-advances

1 Introduction

Climate change due to anthropogenic greenhouse gas (GHG) emissions is the foremost scientific and technological challenge of the 21st century. In 2024, global temperatures exceeded 1.5 °C relative to the pre-industrial 1990 baseline for the first time, with clear – and devastating – consequences from an increased prevalence of extreme weather events.[1] The majority of GHG emissions come from burning fossil fuels for energy, and achieving net zero emissions is key to mitigating climate change. This requires significant changes to how we produce and consume energy. In 2023, the US produced 27.4 Petawatt hours (PWh) of energy, with 82.4% derived from fossil fuels. Of this, only 34.5% was used in energy services, and the remaining 65.7% was lost as waste heat.[2–4] This scale of energy waste means that technologies to improve energy efficiency are an important enabler of net zero.

Thermoelectric (TE) power harnesses the Seebeck effect in a TE material to converts heat to electricity and thus recover waste heat as electrical energy. A thermoelectric generator (TEG) combines two TE materials with dominant p-type (hole) and n-type (electron) carriers, connected electrically in series and thermally in parallel, to harvest electrical energy from the temperature gradient between a heat source and sink. TEGs are solid state devices with no moving parts, are maintenance free and easily scalable, and produce no noise or emissions during operation, making them suitable for a wide range of applications. These include, but are not limited to: battery-free power sources for wireless sensors, wearables and medical devices;[5–7] heat recovery from automobile powertrains and data centres;[8,9] and as a primary geothermal power source.[10] The conversion efficiency of a TE material is typically measured by the dimensionless figure of merit *zT*:

$$zT = \frac{S^2\sigma T}{\kappa_{el} + \kappa_{latt}} \quad (1)$$

A large *zT* requires a high (absolute) Seebeck coefficient $|S|$ and electrical conductivity σ to optimise the power factor $S^2\sigma$ (PF), and a low electronic and lattice thermal conductivity $\kappa = \kappa_{latt} + \kappa_{el}$. High σ is characteristic of metals, whereas large $|S|$ is typically associated with semiconductors and insulators, and low κ is associated with amorphous materials (glasses). The optimum physical properties for high-performance TEs therefore straddle three traditionally distinct classes of material. The three electrical properties are a product of the electronic structure, and the σ/κ_{el} and $|S|$ are typically proportional and inversely proportional, respectively, to the charge carrier concentration *n*.[11] The κ_{latt} depends on the structure and chemical bonding and is typically minimised in materials composed of heavy elements, with weak chemical bonding, and/or with features such as "active" lone pairs that lead to strong phonon anharmonicity.[12,13]

Currently, the most widely used thermoelectric (TE) materials are Bi_2Te_3 for near-room temperature applications (*zT* from ~1–1.5 at 350–450 K)[4,14–16] and PbTe for high-temperature power generation (*zT* up to 2.2 at 915 K),[17] due to a combination

Department of Chemistry, University of Manchester, Oxford Road, Manchester M13 9PL, UK. E-mail: jonathan.skelton@manchester.ac.uk

of a favourable electronic structure and intrinsically low thermal conductivity.[18,19] However, Te is scarce and the environmental toxicity of Pb raises potential concerns over end-of-life disposal, which restrict these materials to niche applications.[20] Widespread adoption of TEGs thus requires alternative materials that balance high performance with sustainability and cost efficiency.

Oxides are attractive candidate thermoelectric materials due to their low toxicity, low cost, and exceptional chemical stability, the latter of which makes them particularly well suited to high temperature heat recovery in automotive and industrial settings. Oxides often exhibit intrinsically large Seebeck coefficients, but typically also suffer from low electrical conductivity and high lattice thermal conductivity, resulting in overall modest zT values. However, the discovery of high thermoelectric power factors in cobalt oxides in the 1990s led to the identification of several families of prospective oxide TEs. p-type oxides include the layered cobaltites Na_xCoO_2,[21–24] $Ca_3Co_4O_9$,[25–27] and $Bi_2Sr_2Co_2O_y$.[28–30] n-type oxides include ZnO[31] and the ABO_3 oxide perovskites, in particular $SrTiO_3$[32–34] (STO) and $CaMnO_3$.[35,36]

$SrTiO_3$ in particular has emerged as one of the most promising oxide perovskite TEs due to its chemical versatility, high thermal stability, and tunable electronic properties.[37] Compared to the related $CaTiO_3$ and $BaTiO_3$, STO has an intrinsically large $|S|$, reasonable σ, superior PF, and impressive thermal stability at elevated temperature.[37–41] Computational modelling has further determined that these advantageous properties are due to STO supporting a significantly higher σ while maintaining comparable $|S|$ to other titanates.[42,43]

STO is typically prepared and tested in thin-film form, with high-temperature zT competitive with other benchmark thin-film systems, *e.g.* $zT \approx 0.29$ at $T = 1000$ K in $Sr(Ti_{0.8}Nb_{0.2})O_{2.75}$[44] *vs.* $zT \approx 0.3$ in Sb_2Te_3,[45] $zT \approx 0.45$ in unoptimised SnSe,[46] and $zT \approx 0.4$ in carbon nanotube films.[47] Control of nanostructure can potentially push this much higher, with an unprecedented $zT \approx 1.6$ at $T = 298$ K recently reported for $Sr(Ti_{0.8}Nb_{0.2})O_3$ through precisely controlled strain and interfacial polarisation.[48] This is significantly higher than the $zT = 0.02$–0.08 obtained for bulk STO at room temperature, where the large $\kappa = 9$–12 W m^{-1} K^{-1} limits the thermoelectric performance.[49]

The wide variation in experimental results is in part due to the high structural and chemical flexibility inherent to perovskites, which can adopt multiple crystal phases and can accommodate doping at the A and B cation sites as well as significant levels of oxygen deficiency. Optimising STO and other oxide perovskite thermoelectrics therefore requires a good fundamental understanding of the underlying structure–property relationships. In a previous study, we applied a fully *ab initio* modelling approach to study the thermoelectric performance of orthorhombic $CaTiO_3$, tetragonal $SrTiO_3$ and rhombohedral $BaTiO_3$.[43] Among our key findings was that the crystal structure had a significant impact on the physical properties and in particular the κ_{latt}. In this work, we build on this with a detailed first-principles study of STO in the orthorhombic, tetragonal and cubic phases. We find that the smaller primitive cell of the $Pm\bar{3}m$ phase results in larger phonon group velocities and high κ_{latt}, whereas the $I4/mcm$ phase shows significantly stronger polar-optic phonon carrier scattering and lower electrical conductivity and power factors. As a result, the hypothetical *Pnma* phase, which combines the lower κ_{latt} of the tetragonal phase and the high PF of the cubic phase, is predicted to show a $\sim$25% larger zT than the cubic phase and $\sim$50% larger zT than the tetragonal phase at high temperature. This work therefore demonstrates that materials engineering strategies to stabilise particular structural distortions from the cubic aristotype could be a facile route to optimising the performance of STO and other oxide perovskite thermoelectrics.

2 Computational modelling

2.1 Prediction of thermoelectric properties

2.1.1 Lattice thermal conductivity. The lattice thermal conductivity due to "particle-like" heat transport through phonons, $\boldsymbol{\kappa}_p$, was initially calculated by solving the phonon Boltzmann transport equation (BTE) within the single-mode relaxation-time approximation (SM-RTA).[50]

In the SM-RTA, the macroscopic $\boldsymbol{\kappa}_p$ is obtained as an average over contributions $\boldsymbol{\kappa}_{\boldsymbol{qj}}$ from microscopic phonon modes $\boldsymbol{qj}$, with wavevector $\boldsymbol{q}$ and band index j:[50]

$$\boldsymbol{\kappa}_p(T) = \frac{1}{N_{\boldsymbol{q}} V}\sum_{\boldsymbol{qj}} \boldsymbol{\kappa}_{\boldsymbol{qj}} = \frac{1}{N_{\boldsymbol{q}} V}\sum_{\boldsymbol{qj}} C_{\boldsymbol{qj}}(T)\boldsymbol{v}_{\boldsymbol{qj}} \otimes \boldsymbol{v}_{\boldsymbol{qj}}\tau_{\boldsymbol{qj}}(T) \quad (2)$$

The normalisation factor is the product of the unit-cell volume V and the number of wavevectors $N_{\boldsymbol{q}}$ included in the summation. The phonon mode heat capacities $C_{\boldsymbol{qj}}$ and group velocities $\boldsymbol{\nu}_{\boldsymbol{qj}}$ are calculated from the harmonic phonon frequencies $\omega_{\boldsymbol{qj}}$ as:

$$C_{\boldsymbol{qj}}(T) = k_B\left(\frac{\hbar\omega_{\boldsymbol{qj}}}{k_B T}\right)^2 n_{\boldsymbol{qj}}(T)\left(n_{\boldsymbol{qj}}(T)+1\right) \quad (3)$$

$$\boldsymbol{v}_{\boldsymbol{qj}} = \frac{\partial\omega_{\boldsymbol{qj}}}{\partial \boldsymbol{q}} \quad (4)$$

The $n_{\boldsymbol{qj}}$ in eqn (3) are the Bose–Einstein occupation numbers given by:

$$n_{\boldsymbol{qj}}(T) = \frac{1}{\exp\left[\hbar\omega_{\boldsymbol{qj}}/k_B T\right]-1} \quad (5)$$

The phonon lifetimes $\tau_{\boldsymbol{qj}}$ are determined from the inverse of the phonon linewidths (scattering rates) $\Gamma_{\boldsymbol{qj}}$:

$$\tau_{\boldsymbol{qj}}(T) = \frac{1}{\Gamma_{\boldsymbol{qj}}(T)} \quad (6)$$

The linewidths are calculated using third-order perturbation theory as outlined in ref. 50, with the $\Gamma_{\boldsymbol{qj}}$ obtained as a sum of contributions from anharmonic energy- and (crystal) momentum-conserving three-phonon scattering processes.

The SM-RTA model in eqn (2) only considers phonon depopulation events, whereas in real materials the flow of thermal energy can result in repopulation.[51] This additional contribution can be taken into account by full solution of the linearised Boltzmann transport equation (LBTE).[51,52]

Furthermore, significant overlap between phonon modes, due to small interband frequency spacing and/or to short τ_{qj} (broad Γ_{qj}) can lead to heat conduction through "wave-like" interband tunnelling characteristic of amorphous materials (glasses).[51] This additional contribution $\boldsymbol{\kappa}_{\mathrm{w}}$ can be obtained by solving the Wigner transport equation using the approach outlined in ref. 51. The $\boldsymbol{\kappa}_{\mathrm{w}}$ can then be combined with either the RTA or LBTE models for the $\boldsymbol{\kappa}_{\mathrm{p}}$ to compute the total lattice thermal conductivity as:

$$\boldsymbol{\kappa}_{\mathrm{latt}}(T) = \boldsymbol{\kappa}_{\mathrm{p}}(T) + \boldsymbol{\kappa}_{\mathrm{w}}(T) \tag{7}$$

The $\boldsymbol{\kappa}_{\mathrm{p}}$, $\boldsymbol{\kappa}_{\mathrm{w}}$ and $\boldsymbol{\kappa}_{\mathrm{latt}}$ are 3×3 tensors, with the transport along the three Cartesian directions $\alpha = x, y$ and z given by the diagonal elements $\kappa_{\alpha\alpha}$. As thermoelectric materials typically take the form of consolidated powders or thin films with randomly-oriented crystal grains, we compute a (scalar) average κ_{latt} from:

$$\kappa = \frac{1}{3}\mathrm{Tr}[\boldsymbol{\kappa}] = \frac{1}{3}\left[\kappa_{xx} + \kappa_{yy} + \kappa_{zz}\right] \tag{8}$$

where Tr denotes the trace of the $\boldsymbol{\kappa}$ tensor. We distinguish the scalar and tensor quantities respectively using Roman and bold type.

2.1.2 Electrical conductivity, Seebeck coefficient and electronic thermal conductivity. The electrical conductivity $\boldsymbol{\sigma}$, Seebeck coefficient $\boldsymbol{S}$ and electronic thermal conductivity $\boldsymbol{\kappa}_{\mathrm{el}}$ were determined by solving the electron BTE within the momentum relaxation-time approximation (MRTA).[53,54]

The spectral conductivity $\boldsymbol{\Sigma}$ is calculated according to:[54]

$$\boldsymbol{\Sigma}(\varepsilon, T) = \sum_j \int \frac{1}{8\pi^3} \boldsymbol{v}_{kj} \otimes \boldsymbol{v}_{kj} \tau_{kj}(T) \delta\left[\varepsilon - \varepsilon_{kj}\right] \mathrm{d}\boldsymbol{k} \tag{9}$$

The summation and integral run over electronic states $\boldsymbol{kj}$, with wavevector $\boldsymbol{k}$ and band index j, band energy ε_{kj}, group velocity $\boldsymbol{\nu}_{kj}$ and lifetime τ_{kj}. The $\boldsymbol{\nu}_{kj}$ are given by the gradient of the electronic band structure as:

$$\boldsymbol{v}_{kj} = \frac{\partial \varepsilon_{kj}}{\partial \boldsymbol{k}} \tag{10}$$

The τ_{kj} are calculated by combining approximate models of the electron scattering rates from acoustic deformation potential (ADP), polar-optic phonon (POP), ionised impurity (IMP) and piezoelectric (PIE) scattering using Matthiessen's rule:[54]

$$\tau_{kj}^{-1}(T) = \Gamma_{kj}^{\mathrm{ADP}}(T) + \Gamma_{kj}^{\mathrm{POP}}(T) + \Gamma_{kj}^{\mathrm{IMP}}(T) + \Gamma_{kj}^{\mathrm{PIE}}(T) \tag{11}$$

Expressions for the scattering rates can be found in ref. 54.

The $\boldsymbol{\Sigma}$ is then used to obtain the generalised moments of the transport distribution function, $\mathscr{L}^n$, from:

$$\mathscr{L}^n(\varepsilon_{\mathrm{F}}, T) = e^2 \int \boldsymbol{\Sigma}(\varepsilon, T)(\varepsilon - \varepsilon_{\mathrm{F}})^n \left[-\frac{\partial f^0(\varepsilon, \varepsilon_{\mathrm{F}}, T)}{\partial \varepsilon}\right] \mathrm{d}\varepsilon \tag{12}$$

where ε_{F} is the Fermi energy and f^0 is the Fermi–Dirac distribution function:

$$f^0(\varepsilon, \varepsilon_{\mathrm{F}}, T) = \frac{1}{\exp[(\varepsilon - \varepsilon_{\mathrm{F}})/k_{\mathrm{B}}T] + 1} \tag{13}$$

Finally, the $\boldsymbol{\sigma}$, $\boldsymbol{S}$ and $\boldsymbol{\kappa}_{\mathrm{el}}$ are calculated from the $\mathscr{L}^n(T)$ according to:[53,54]

$$\boldsymbol{\sigma}(\varepsilon_{\mathrm{F}}, T) = \mathscr{L}^0(\varepsilon_{\mathrm{F}}, T) \tag{14}$$

$$\boldsymbol{S}(\varepsilon_{\mathrm{F}}, T) = \frac{1}{eT}\frac{\mathscr{L}^1(\varepsilon_{\mathrm{F}}, T)}{\mathscr{L}^0(\varepsilon_{\mathrm{F}}, T)} \tag{15}$$

$$\boldsymbol{\kappa}_{\mathrm{el}}(\varepsilon_{\mathrm{F}}, T) = \frac{1}{e^2 T}\left[\frac{\left(\mathscr{L}^1(\varepsilon_{\mathrm{F}}, T)\right)^2}{\mathscr{L}^0(\varepsilon_{\mathrm{F}}, T)} - \mathscr{L}^2(\varepsilon_{\mathrm{F}}, T)\right] \tag{16}$$

The $\mathscr{L}^n$, and hence the $\boldsymbol{\sigma}$, $\boldsymbol{S}$ and $\boldsymbol{\kappa}_{\mathrm{el}}$, depend on the Fermi energy. Under the assumption that dopants do not affect the host band structure, the ε_{F} can be adjusted to specify an extrinsic carrier concentration ("doping level") n to predict the effect of chemical doping. (This is termed the "rigid band approximation" (RBA).)

As for the $\boldsymbol{\kappa}_{\mathrm{latt}}$, the $\boldsymbol{\sigma}$, $\boldsymbol{S}$ and $\boldsymbol{\kappa}_{\mathrm{el}}$ are 3×3 tensors, and scalar averages σ, S and κ_{el} can be obtained in an analogous manner to eqn (8). The power factor $S^2\sigma$ in eqn (1) is also orientation dependent, and the PF along a given Cartesian direction can be calculated from:

$$(S^2\sigma)_\alpha = {S_{\alpha\alpha}}^2 \sigma_{\alpha\alpha} \tag{17}$$

The scalar average PF is obtained in the same way, but using the averaged S and σ to match how this quantity is evaluated from experimental measurements (*i.e.* we do not form and take the diagonal average of a "PF tensor").

2.1.3 Thermoelectric figure of merit. The calculated $\boldsymbol{\kappa}_{\mathrm{latt}}$ and $\boldsymbol{\sigma}$, $\boldsymbol{S}$ and $\boldsymbol{\kappa}_{\mathrm{el}}$ can be combined to determine the thermoelectric figure of merit zT from first principles using eqn (1). The $\boldsymbol{\kappa}_{\mathrm{latt}}$ is a function of temperature, while the three electrical properties are a function of both T and the Fermi energy ε_{F} (extrinsic carrier concentration n; *cf.* eqn (7) and eqn (14)–(16)). We therefore determine the zT as a (two-dimensional) function of both T and n.

The zT is orientation dependent and the values along the three Cartesian directions can be calculated as:

$$(zT)_\alpha = \frac{{S_{\alpha\alpha}}^2 \sigma_{\alpha\alpha} T}{\kappa_{\mathrm{el},\alpha\alpha} + \kappa_{\mathrm{latt},\alpha\alpha}} \tag{18}$$

As for the power factor, the scalar average zT is calculated using the scalar averages of the four constituent properties, as opposed to the diagonal average of a "zT tensor").

As noted in Section 2.1.1, heat transport through three different mechanisms can be taken into account when computing the $\boldsymbol{\kappa}_{\mathrm{latt}}$ (particle-like transport with the SM-RTA or LBTE models, and interband tunnelling). We discuss the contributions of these different mechanisms in detail in Section 3.1 below.

2.2 Density-functional theory calculations

Calculations were performed using pseudopotential plane wave density functional theory (DFT) as implemented in the Vienna *ab initio* simulation package (VASP) code.[55]

Initial structures of $SrTiO_3$ in the tetragonal $I4/mcm$ and cubic $Pm\bar{3}m$ phases were taken from the materials project (MP) database[56] (mp-5229, mp-4651), and an orthorhombic $Pnma$ structure was built by substituting the A-site cation in $CaTiO_3$ (mp-1185232). All three structures were then fully optimised to

tight tolerances of 10^{-8} eV on the total energy and 10^{-3} eV Å^{-1} on the forces.

Electron exchange and correlation were modelled using the PBEsol generalised gradient approximation (GGA) functional.[57] The ion cores were modelled using projector-augmented (PAW) pseudopotentials[58,59] with the following valence configurations: Ti – $3d^2\ 4s^2$; O – $2s^2\ 2p^4$; Sr – $4s^2\ 4p^6\ 5s^2$. The valence wavefunctions were described using a plane-wave basis with an 800 eV kinetic-energy cutoff, and the electronic Brillouin zones were sampled using Γ-centred Monkhorst–Pack ***k***-point meshes[60] with $6 \times 6 \times 6$, $5 \times 5 \times 3$ and $3 \times 2 \times 4$ subdivisions for the $Pm\bar{3}m$, $I4/mcm$ and *Pnma* phases respectively. These parameters were chosen based on explicit testing to converge the absolute total energies to <1 meV atom^{-1} and the external pressures to <1 kbar (0.1 GPa).

2.2.1 Lattice dynamics and thermal conductivity. Lattice-dynamics and thermal-conductivity calculations were performed using the supercell finite-differences approach implemented in the Phonopy and Phono3py codes.[50,61] The 2nd-order (harmonic) force constants were computed in $4 \times 4 \times 4$ expansions of the $Pm\bar{3}m$ unit cell and $I4/mcm$ primitive cell (320/640 atoms), and a $4 \times 2 \times 4$ expansion of the *Pnma* unit cell (640 atoms). Atom-projected phonon density of states (PDoS) curves were computed by interpolating the phonon frequencies onto regular Γ-centred ***q***-point grids with $12 \times 12 \times 12$ subdivisions using the linear tetrahedron method for Brillouin-zone integration. Phonon dispersions were obtained by evaluating the frequencies at strings of ***q*** points passing through the high-symmetry points in the respective Brillouin zones. Non-analytical corrections to the dynamical matrices at $\boldsymbol{q} \rightarrow \Gamma$ were included with the approach in ref. 62 using Born effective-charge tensors $\boldsymbol{Z}^*$ and high-frequency dielectric constants $\boldsymbol{\varepsilon}_\infty$ computed from density-functional perturbation theory (DFPT).[63]

The 3rd-order (anharmonic) force constants were computed in a $3 \times 3 \times 3$ expansion of the $Pm\bar{3}m$ unit cell (135 atoms), a $2 \times 2 \times 2$ expansion of the $I4/mcm$ primitive cell (80 atoms), and a $2 \times 1 \times 2$ expansion of the *Pnma* unit cell (80 atoms). The "particle-like" lattice thermal conductivities for band transport were calculated using the SM-RTA model by combining the 2nd- and 3rd-order force constants to evaluate the heat capacities $C_{\boldsymbol{q}j}$, group velocities $\boldsymbol{\nu}_{\boldsymbol{q}j}$ and lifetimes $\tau_{\boldsymbol{q}j}$ on uniform Γ-centred $22 \times 22 \times 22$, $8 \times 8 \times 8$ and $12 \times 12 \times 12$ ***q***-point sampling meshes for the $Pm\bar{3}m$, $I4/mcm$ and *Pnma* phases respectively. These meshes were chosen based on explicit testing to converge the scalar average of the $\boldsymbol{\kappa}_p$ tensors (eqn (2) and (8)) to within 5% of the values obtained with larger sampling meshes. We also solved the full linearised phonon BTE to obtain the $\boldsymbol{\kappa}_p$ including repopulation effects, and the Wigner transport equation to determine the $\boldsymbol{\kappa}_w$ contribution from interband tunnelling.[51]

2.2.2 Electronic transport. Electronic transport calculations were performed using the AMSET code.[54] Accurate band gaps E_g were obtained from non-self-consistent calculations with the HSE06 hybrid functional.[64,65] These calculations were also used to obtain electronic PDoS curves using a Gaussian smearing with a width σ = 0.01 eV. Uniform band-structure calculations were then performed with PBEsol and denser $12 \times 12 \times 12$, $10 \times 10 \times 6$, and $6 \times 4 \times 8$ ***k***-point meshes for the $Pm\bar{3}m$, $I4/mcm$ and *Pnma* phases, respectively, and the band-gaps increased to the HSE06 values using scissors operators. These meshes were further interpolated to approx. 20×, 30× and 10× higher densities when calculating the electrical transport properties. The charge densities from the calculations were also used to calculate the band energies at strings of ***k***-points along the high-symmetry paths in the Brillouin zones to obtain electronic band structures, with the band gaps again corrected using scissors operators. The combined band structure and PDoS curves were plotted using sumo.[66]

AMSET estimates the electronic relaxation times by summing scattering rates from four different processes, *viz.* acoustic deformation potential (ADP), polar optic phonon (POP), piezoelectric (PIE), and ionised impurity (IMP) scattering, requiring a range of material properties to be calculated. (We note that PIE scattering is negligible in the three systems examined in this work, as they have centrosymmetric space groups and the piezoelectric moduli vanish by symmetry.)

Deformation potentials were computed by performing a series of single-point energy calculations on deformed structures, generated using AMSET, with PBEsol. The high-frequency, ionic and static dielectric constants $\boldsymbol{\varepsilon}_\infty$, $\boldsymbol{\varepsilon}_{ionic}$ and $\boldsymbol{\varepsilon}_s = \boldsymbol{\varepsilon}_\infty + \boldsymbol{\varepsilon}_{ionic}$, together with the Born effective charges $\boldsymbol{Z}^*$ and piezoelectric moduli, were determined using DFPT.[63] Explicit tests found that 2× ($Pm\bar{3}m$/*Pnma* phases) and 3× denser ***k***-point sampling ($I4/mcm$ phase) compared to the "base" meshes used for geometry optimisation were required to converge the $\boldsymbol{\varepsilon}_\infty$. The $\boldsymbol{Z}^*$ were used to determine the infrared (IR) activities of the phonon modes at $\boldsymbol{q} = \Gamma$,[67,68] evaluated with Phonopy, and to calculate the polar optic phonon (POP) frequency ω_{po}. Finally, the elastic constant matrix elements C_{ij} were computed using PBEsol and the finite-differences routines in VASP[69] (denser ***k***-point sampling was not required for these calculations).

3 Results and discussion

3.1 Structure, phonon spectra and lattice thermal conductivity

The optimised structures of the three $SrTiO_3$ phases are shown in Fig. 1. For all three systems the lattice parameters are in excellent agreement with experimental measurements, with maximum differences of 0.55% in the lattice parameters and 0.42% in the unit cell volumes of the $Pm\bar{3}m$ and $I4/mcm$ phases (Table S1). We note that the hypothetical *Pnma* phase of STO has not been observed experimentally, but is adopted by heavily-doped derivatives, and our predicted lattice parameters and cell volumes are within 0.56 and 1.58%, respectively, of the measurements on $SrTi_{0.9}Fe_{0.1}Ta_{0.1}O_3$ reported in ref. 70.

Both the lower-symmetry tetragonal $I4/mcm$ and orthorhombic *Pnma* phases can be generated from the "parent" $Pm\bar{3}m$ structure by rotations of the TiO_6 octahedra.[71] The $I4/mcm$ phase is obtained by an anti-phase tilt of successive "layers" of TiO_6 octahedra around the z axis, such that the a, b and c lattice vectors of the $I4/mcm$ structure correspond to the (110), ($\bar{1}$10) and (002) directions in the cubic phase. The *Pnma* phase is obtained by a more complex combination of an in-phase tilt

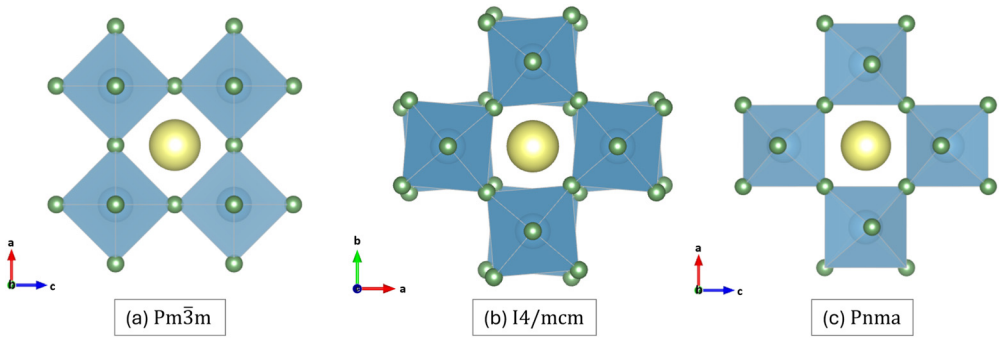

Fig. 1 Optimised structures of $SrTiO_3$ in the cubic $Pm\bar{3}m$ (a), tetragonal $I4/mcm$ (b) and orthorhombic $Pnma$ phase (c). The $I4/mcm$ and $Pnma$ structures are oriented to show the equivalence to the cubic structure.[71] The Sr, Ti and O atoms are shown in yellow, light blue and green respectively. These images were prepared using the VESTA software.[72]

around x and anti-phase tilts of the same angle around y and z, and the a, b and c lattice vectors correspond to the (011), (020) and (01$\bar{1}$) directions in the $Pm\bar{3}m$ parent.

The calculated phonon spectra of the three $SrTiO_3$ phases are shown in Fig. 2. The cubic $Pm\bar{3}m$ structure has $n_a = 5$ atoms in the primitive cell, resulting in $3n_a = 15$ branches at each phonon wavevector $\boldsymbol{q}$. In contrast, the $I4/mcm$ and $Pnma$ structures have $n_a = 10$ and 20, respectively, and thus considerably more complex phonon spectra with 30 and 60 bands per $\boldsymbol{q}$. The increase in complexity due to the larger primitive unit cells is further compounded by the lower band degeneracy from the reduced symmetry.

In all three systems, the A-site cation makes the largest contribution to the low-frequency modes, with sharp features in the DoS consistent with some degree of "rattling" behaviour. The mid-frequency optic modes are predominantly due to the motion of the Ti and O atoms, and can be attributed to deformations of the TiO_6 octahedra, while all three systems show prominent high-frequency features associated with motion of the O atoms. The calculated phonon spectra of the $Pm\bar{3}m$ and $I4/mcm$ phases agree well with previous calculations.[73,74]

With the exception of some small interpolation artefacts around $\boldsymbol{q} = \Gamma$ in the $Pnma$ dispersion, the dispersions of the orthorhombic and tetragonal phases show no imaginary harmonic modes, indicating that both structures are dynamically stable. On the other hand, the dispersion of the $Pm\bar{3}m$ phase shows prominent dynamical instabilities at $\boldsymbol{q} = R$ and M, in agreement with previous calculations.[75,76] These off-Γ instabilities are related to the octahedral tilts that generate the lower-symmetry structures.[77] We were not able to find reference phonon spectra for the $Pnma$ phase, but the good agreement for the $Pm\bar{3}m$ and $I4/mcm$ phases compared to previous studies gives us confidence in our calculations on the orthorhombic phase.

The scalar-average "particle-like" conductivity, κ_p, of the three $SrTiO_3$ phases obtained using the single-mode relaxation-time approximation (SM-RTA) are compared in Fig. 3(a), and values at $T = 1000$ K are compared in Table 1. At 1000 K, we predict $\kappa_p = 1.2$–1.9 W m^{-1} K^{-1}, with an ordering of $Pm\bar{3}m > I4/mcm > Pnma$. Compared to the intermediate $I4/mcm$ phase, which we examined in our previous study,[43] the lower-symmetry orthorhombic phase has a 13% lower κ_p, but the κ_p is still 26% larger than that of the isostructural $CaTiO_3$ (0.96 W m^{-1} K^{-1}). On the other hand, the high-symmetry $Pm\bar{3}m$ phase has a 34% higher κ_p than the $I4/mcm$ phase. Taken together, this suggests the effects of crystal symmetry and A-site cation mass on the κ_p are both strong and of similar magnitude. On the other hand, the three phases of STO have very similar density $\rho = 5.1$–5.12 g cm^{-3} (Table S1), which in our view cannot explain the significant variation in the κ_p. This provides further support for crystal symmetry being the key factor in the reduction in κ_p from the cubic to the orthorhombic phase.

To explore the origin of the differences in the SM-RTA κ_p, we employ the analysis from our previous studies[13] and define a weighted-average phonon lifetime τ^{ph} such that the κ_p can be written:

$$\begin{aligned}\kappa_p(T) &= \tau^{ph}(T) \times \frac{1}{N_{\boldsymbol{q}} V} \sum_{\boldsymbol{q}j} \frac{\kappa_{\boldsymbol{q}j}(T)}{\tau_{\boldsymbol{q}j}(T)} \\ &= \tau^{ph}(T) \times \frac{1}{N_{\boldsymbol{q}} V} \sum_{\boldsymbol{q}j} C_{\boldsymbol{q}j}(T) \frac{1}{3} \mathrm{Tr}\left[\boldsymbol{v}_{\boldsymbol{q}j} \otimes \boldsymbol{v}_{\boldsymbol{q}j}\right]\end{aligned} \tag{19}$$

where we have taken the scalar average of the group velocity outer product (*cf.* eqn (8)). The summation κ_p/τ^{ph} is temperature dependent due to the heat capacities $C_{\boldsymbol{q}j}$ and the high-temperature saturation value provides a metric for comparing differences in group velocities between materials, while the τ^{ph} can be used to compare phonon lifetimes.[13]

The κ_p/τ^{ph} and τ^{ph} as a function of temperature for the three phases of STO are compared in Fig. 3(b) and (c), respectively, and values at $T = 1000$ K are listed in Table 1. The calculated κ_p/τ^{ph} of the $Pnma$ and $I4/mcm$ phases are similar, differing by only 3.8% at 1000 K, whereas the group velocities of the $Pm\bar{3}m$ phase are around a factor of two larger. Given that the group velocities $\boldsymbol{\nu}_{\boldsymbol{q}j}$ are the gradient of the phonon dispersion, this difference can be attributed to the impact of the smaller primitive cell of the cubic phase on the phonon dispersion (*cf.* eqn (4), Fig. 2). On the other hand, the τ^{ph} fall in the order $Pm\bar{3}m < Pnma < I4/mcm$, *i.e.* the cubic phase has the shortest averaged phonon lifetimes. The τ^{ph} of the $Pnma$ phase is 17% shorter than the $I4/mcm$ phase at 1000 K, resulting in a lower overall κ_p, whereas the much larger κ_p/τ^{ph} of the $Pm\bar{3}m$ phase offsets the short τ^{ph} and results in the largest predicted κ_{latt} among all three phases.

In the SM-RTA, the phonon lifetimes $\tau_{\boldsymbol{q}j}$ are calculated as the inverse of the linewidths $\Gamma_{\boldsymbol{q}j}$, which are obtained perturbatively

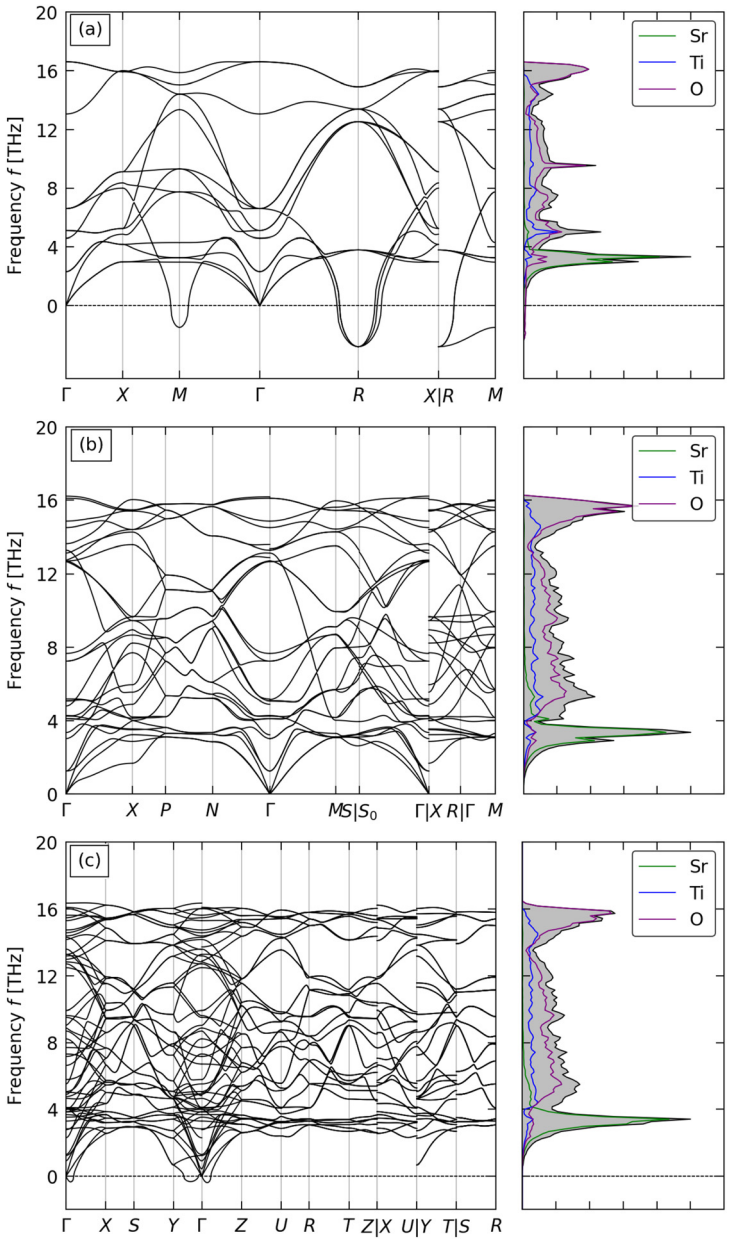

Fig. 2 Calculated phonon dispersion and density of states (DoS) of $Pm\bar{3}m$ (a), $I4/mcm$ (b) and $Pnma$ $SrTiO_3$ (c). The DoS curves show the total DoS in black/grey with the projections onto the Sr, Ti and O atoms in green, blue and purple respectively.

from the imaginary parts of the phonon self-energies.[50] The $\Gamma_{\boldsymbol{q}j}$ can be written approximately as:

$$\tilde{\Gamma}_{\boldsymbol{q}j}(T) = 2 \times \frac{18\pi}{\hbar^2} P_{\boldsymbol{q}j} N_2(\boldsymbol{q}, \omega_{\boldsymbol{q}j}, T) \tag{20}$$

The $P_{\boldsymbol{q}j}$ are the averaged three-phonon interaction strengths $\Phi_{\boldsymbol{q}j,\boldsymbol{q}'j',\boldsymbol{q}''j''}$ given by:

$$P_{\boldsymbol{q}j} = \frac{1}{(3n_a)^2} \sum_{\boldsymbol{q}'j',\boldsymbol{q}''j''} \left|\Phi_{\boldsymbol{q}j,\boldsymbol{q}'j',\boldsymbol{q}''j''}\right|^2 \tag{21}$$

The function $N_2(\boldsymbol{q},\omega,T)$ defines the "scattering phase space", *i.e.* the number of energy- and momentum-conserving scattering pathways available to a phonon with wavevector $\boldsymbol{q}$ and frequency ω at temperature T:

$$N_2(\boldsymbol{q}, \omega, T) = N_2^{(1)}(\boldsymbol{q}, \omega, T) + N_2^{(2)}(\boldsymbol{q}, \omega, T) \tag{22}$$

The functions $N_2^{(1)}$ and $N_2^{(2)}$ define separately the phase spaces for collision/coalescence (Type 1, two phonons → one phonon) and decay/emission events (Type 2, 1 → 2) and are given by:

$$\begin{aligned} N_2^{(1)}(\boldsymbol{q}, \omega, T) = & \frac{1}{N_{\boldsymbol{q}}} \sum_{\boldsymbol{q}'j',\boldsymbol{q}''j''} \Delta(-\boldsymbol{q} + \boldsymbol{q}' + \boldsymbol{q}'') \\ & \times \left[n_{\boldsymbol{q}'j'}(T) - n_{\boldsymbol{q}''j''}(T)\right] \\ & \times \left[\delta(\omega + \omega_{\boldsymbol{q}'j'} - \omega_{\boldsymbol{q}''j''}) - \delta(\omega - \omega_{\boldsymbol{q}'j'} + \omega_{\boldsymbol{q}''j''})\right] \end{aligned} \tag{23}$$

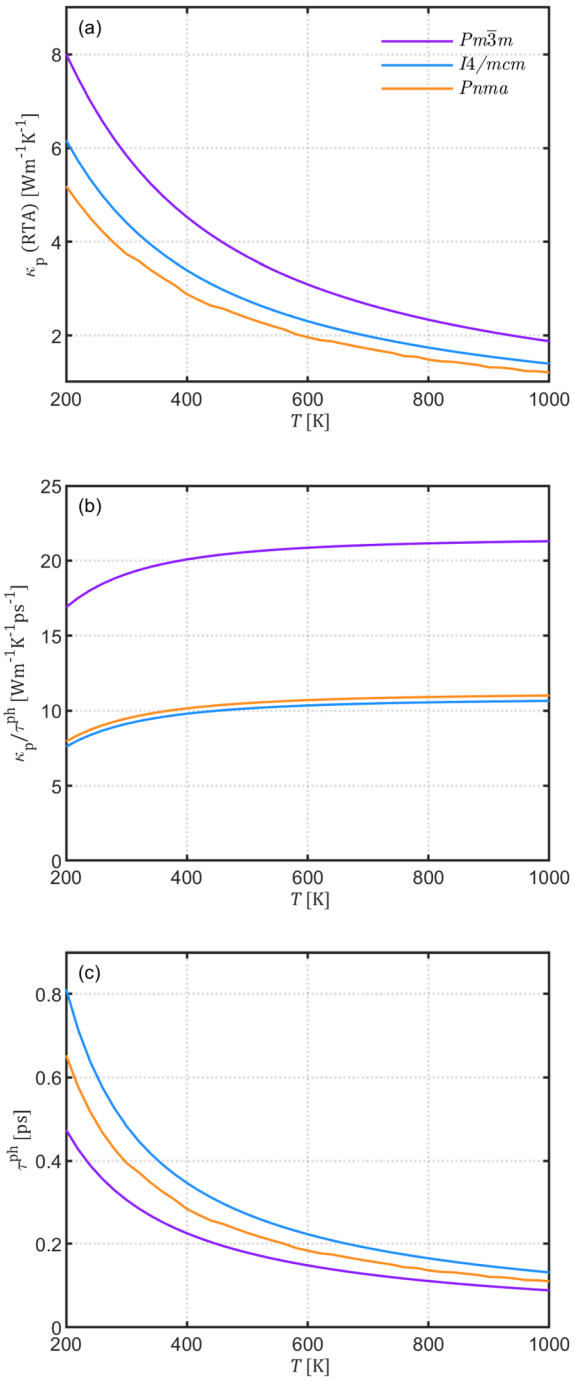

Fig. 3 "Particle-like" (band transport) contributions κ_p to the averaged lattice thermal conductivity κ_{latt} of the $Pm\bar{3}m$, $I4/mcm$ and $Pnma$ phases of $SrTiO_3$ (eqn (2)).[50] Plot (a) shows the scalar-average κ_p, calculated using eqn (8), while plots (b) and (c) show the decomposition into the harmonic summation κ_p/τ^{ph} and weighted-average lifetime τ^{ph} defined in eqn (19).[13]

$$N_2^{(2)}(\boldsymbol{q},\omega) = \frac{1}{N_{\boldsymbol{q}}}\sum_{\lambda'\lambda''}\Delta(-\boldsymbol{q}+\boldsymbol{q}'+\boldsymbol{q}'') \times \left[n_{\boldsymbol{q}'j'}(T)+n_{\boldsymbol{q}''j''}(T)+1\right]\times\delta\left(\omega-\omega_{\boldsymbol{q}'j'}-\omega_{\boldsymbol{q}''j''}\right) \quad (24)$$

where the functions Δ and δ enforce the conservation of (crystal) momentum and energy, respectively. The three-phonon interaction strengths are determined from the harmonic frequencies and displacement vectors (eigenvectors) and the 3rd-order force constants $\boldsymbol{\Phi}^{(3)}$, while the N_2 depend on the harmonic frequencies only. With reference to eqn (20), the average phonon lifetimes can therefore be interpreted in terms of a parameter $\tilde{P}$, describing the average strength of the three-phonon interactions and the level of phonon anharmonicity, and the size of the scattering phase space.[13]

To simplify the comparison between systems, it is useful to average the N_2 over $\boldsymbol{q}$ to obtain functions of frequency only, *i.e.*:

$$\bar{N}_2(\omega,T) = \bar{N}_2^{(1)}(\omega,T)+\bar{N}_2^{(2)}(\omega,T) = \frac{1}{N_{\boldsymbol{q}}}\sum_{\boldsymbol{q}}N_2^{(1)}(\boldsymbol{q},\omega,T)+\frac{1}{N_{\boldsymbol{q}}}\sum_{\boldsymbol{q}}N_2^{(2)}(\boldsymbol{q},\omega,T) \quad (25)$$

Also, whereas the $\tilde{P}$ is a single parameter, and can in principle be compared quantitatively between systems, the $\bar{N}_2$ can only be compared qualitatively. We therefore compute and use one of two metrics to compare the scattering phase spaces.[13] First, we compute the integral of the $\bar{N}_2$, which provides a crude measure of the size of the scattering phase space:

$$\int_0^{\omega_{max}}\bar{N}_2(\omega,T)\mathrm{d}\omega \quad (26)$$

where ω_{max} is the highest frequency in the phonon spectrum.

Secondly, we compute weighted-average $\tilde{N}_2$ calculated from the τ^{ph} and $\tilde{P}$ using eqn (20):

$$\tilde{N}_2 = \frac{\hbar^2}{36\pi}\frac{1}{\tau^{ph}}\frac{1}{\tilde{P}} \quad (27)$$

Finally, we note that for comparison between systems with different n_a the $\tilde{P}$ and $N_2/\bar{N}_2$ need to be multiplied and divided, respectively, by $(3n_a)^2$.

The calculated $\bar{N}_2$ for the $Pm\bar{3}m$ phase of STO at $T = 1000$ K is shown in Fig. 4, and equivalent plots for the $I4/mcm$ and $Pnma$ phases are shown in Fig. S1. We find that the scattering phase space of the low-frequency phonon modes is dominated by collision processes, while decay pathways become available from $\sim$3 THz, are competitive with collisions up to 13 THz, and are the dominant scattering mechanism for the high-frequency modes up to the $f_{max} \approx 16$ THz (*cf.* Fig. 2).

The calculated $\tilde{P}$ and the phase space integral and $\tilde{N}_2$ defined in eqn (26) and (27) for all three phases are listed in Table 1. The scaled $\tilde{P}$ and $\tilde{N}_2$ indicate that the three-phonon scattering strengths and phase spaces are similar across all three phases, with $\tilde{P}$ between 5.08–6.09 $\times$ 10^{-7} eV^2 and $\tilde{N}_2$ between 5.72–7.95 $\times$ 10^{-2} THz^{-1}. The $\tilde{N}_2$ fall in the order of $Pnma \approx I4/mcm < Pm\bar{3}m$, *i.e.* the cubic phase has a notably larger scattering phase space. On the other hand, the $\tilde{P}$ fall in the order $I4/mcm < Pm\bar{3}m < Pnma$. The short τ^{ph} of the cubic phase compared to the other two phases is therefore a product of moderate three-phonon interaction strengths and a large scattering phase space, whereas the longer τ^{ph} of the tetragonal

Table 1 Analysis of the "particle-like" (band transport) contributions κ_p to the scalar-average lattice thermal conductivity κ_{latt} of the three phases of $SrTiO_3$ examined in this work at T = 1000 K. For each κ_p we show the harmonic function κ_p/τ^{ph} and weighted-average lifetime τ^{ph}, defined in eqn (19), together with the integrals of the "scattering phase space" functions $\bar{N}_2$ from 0 to the maximum frequencies ω_{max} in the phonon spectra, the weighted-average three-phonon interaction strengths $\tilde{P}$, and the average number of scattering channels $\tilde{N}_2$, defined in eqn (26), (21) and (27). The latter three quantities are all scaled to allow for comparison between the three phases

	κ_p [W m^{-1} K^{-1}]	κ_p/τ^{ph} [W m^{-1} K^{-1} ps^{-1}]	τ^{ph} [ps]	$\frac{1}{(3n_a)^2}\int_0^{\omega_{max}} \bar{N}_2(\omega)\mathrm{d}\omega$	$\tilde{P} \times (3n_a)^2$ [eV^2]	$\tilde{N}_2/(3n_a)^2$ [THz^{-1}]
Pm$\bar{3}$*m*	1.88	21.29	0.09	2.75×10^{-2}	5.36×10^{-7}	7.95×10^{-2}
*I*4/*mcm*	1.4	10.65	0.13	0.56×10^{-2}	5.08×10^{-7}	5.76×10^{-2}
Pnma	1.21	11.01	0.11	0.16×10^{-2}	6.09×10^{-7}	5.72×10^{-2}

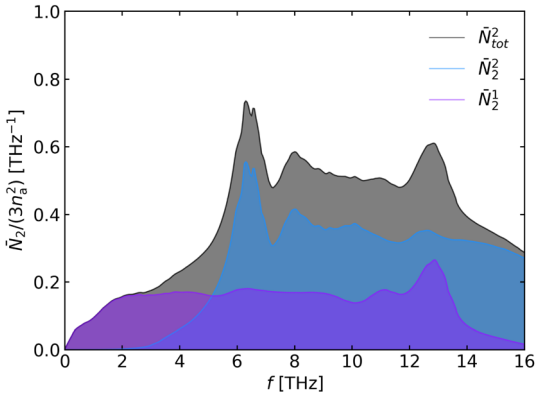

Fig. 4 Average scattering phase space function $\bar{N}_2$ defined in eqn (25) for the *Pm*$\bar{3}$*m* phase of $SrTiO_3$ at T = 1000 K. The separate phase spaces for collision and decay processes ($\bar{N}_2^{(1)}/\bar{N}_2^{(2)}$) are shown in blue and purple, respectively, and the total phase space is shown in grey.

phase is due to comparatively weak three-phonon interactions and a small phase space.

The trend in the κ_p/τ^{ph} with crystal symmetry qualitatively mirrors our previous calculations on the Group IV–VI chalcogenides, including the "flagship" thermoelectric materials SnS and SnSe, where low group velocities were found to be characteristic of low-symmetry structures with large primitive cells.[13] In absolute terms, however, the κ_p/τ^{ph} of all three STO phases are 10–40× larger than chalcogenide phases with comparable symmetry and smaller primitive cells. On the other hand, the τ^{ph} at T = 300 K range from 0.3–0.5 ps (Table S2), placing them on the same order of magnitude as the shortest averaged lifetimes calculated in ref. 13. The $\tilde{N}_2$ at room temperature are on the same order as the largest values obtained for the chalcogenides, while the averaged three-phonon interaction strengths fall within the mid-to-upper range of $\tilde{P}$. Compared to these other flagship thermoelectric materials, the oxides thus have relatively large three-phonon scattering phase spaces, moderate-to-strong phonon anharmonicity, and, consequently, short τ^{ph}.

The trends in the group velocity and lifetimes compared to other classes of materials can be partially interpreted in terms of the chemical bonding. The harmonic frequencies and group velocities are both derived from the 2nd-order force constants (FCs), which describe the changes in atomic forces in response to small displacements of the atoms. Strong chemical bonding favours large FCs, high phonon frequencies, and, consequently, high group velocities (*cf.* eqn (4)). The three-phonon interaction strengths additionally depend on the 3rd-order FCs, which describe the changes in forces in response to pairwise atomic displacements. While we are not aware of any systematic studies to this effect, it is not unreasonable to expect the 2nd- and 3rd-order FCs to be at least loosely correlated, such that stronger bonding results in larger 2nd-order and 3rd-order FCs. From this point of view, the stronger bonding in the oxides results in larger group velocities, but also stronger three-phonon interactions and shorter phonon lifetimes. In these systems, the former dominates the κ_p.

The generality of our finding that the κ_{latt} depends sensitively on crystal structure is also supported by a recent theoretical study of Zintl compounds.[78] In particular, this study found that low group velocities and, in some cases, short lifetimes are favoured by inhomogeneous chemical bonding, for which low crystal symmetry is an indicator, which mirrors the trends for the three phases of $SrTiO_3$ in the present study.

We also compared the κ_p obtained from the SM-RTA in eqn (2) with that obtained by full solution of the linearised phonon Boltzmann transport equation (LBTE) (Table 2).[50,52] The conceptual difference between the two models is that the SM-RTA only considers depopulation events, whereas the LBTE approach also accounts for repopulation. In practice, the full LBTE solution gives similar results to the SM-RTA, with differences between −2.5 and 6.9% in the κ_p at T = 1000 K.

In our previous work on the lanthanide cobalates $LnCoO_3$[79] we found that "wave-like" tunnelling made a significant contribution to the overall κ_{latt}. We find the same for all three phases of $SrTiO_3$, with the κ_w accounting for 33–35% of the κ_{latt} of the *Pm*$\bar{3}$*m* phase at 1000 K, depending on whether the κ_p is calculated using the SM-RTA or LBTE model, and a larger 47–49 and 52–54% of the κ_{latt} of the lower-symmetry *I*4/*mcm* and *Pnma* phases (Table 2). The larger κ_w of the tetragonal and orthorhombic phases can be explained by the more complex phonon dispersions leading to a smaller interband spacing, which more than compensates for the narrower linewidths (longer lifetimes) compared to the cubic phase (*cf.* Fig. 2 and Table 1). While we only considered the *Pnma* phases of the $LnCoO_3$, we predicted a similar ∼50% contribution from the κ_w to the κ_{latt}.[79] We have also found that the κ_w is much more significant in the more structurally-complex "π" phases of the chalcogenides SnS and SnSe than the simpler orthorhombic phases.[80] In conjunction with the present results, this suggests that there may be a universal trade-off between high κ_p in higher-symmetry phases and high κ_w in lower-symmetry phases.

Taken together, our analysis shows that the κ_{latt} of $SrTiO_3$ is a balance of several competing factors. The "particle-like"

Table 2 Contributions to the scalar-average lattice thermal conductivity, $\kappa_{latt} = \kappa_p + \kappa_w$ of the three phases of $SrTiO_3$ examined in this work from "particle-like" conductivity κ_p and "wave-like" (interband tunnelling) conductivity κ_w at T = 1000 K. Values of the κ_p obtained with the single-mode relaxation-time approximation (SM-RTA) and full solution of the linearised Boltzmann transport equation (LBTE) are given, together with the equivalent κ_{latt}

	[W m^{-1} K^{-1}]				
	κ_p (SM-RTA)	κ_p (LBTE)	κ_w	κ_{latt} (SM-RTA)	κ_{latt} (LBTE)
Pm$\bar{3}$*m*	1.88	2.01	1.0	2.88	3.01
*I*4/*mcm*	1.4	1.44	1.32	2.72	2.77
Pnma	1.21	1.18	1.36	2.57	2.54

conductivity, κ_p, is largest in the high-symmetry *Pm*$\bar{3}$*m* phase, where the large phonon group velocities compensate for shorter lifetimes. On the other hand, the interband tunnelling contribution, κ_w, is larger in the lower-symmetry *I*4/*mcm* and *Pnma* phases, where the smaller interband frequency spacing outweighs the narrower linewidths. Overall, however, we predict the *Pm*$\bar{3}$*m* phase to have a 5–10% larger κ_{latt} than the *I*4/*mcm* phase, and a 10–20% larger κ_{latt} than the *Pnma* phase, at 1000 K, and we therefore conclude that the phonon group velocities are the biggest factor in determining the higher thermal conductivity of the cubic phase. The difference between the tetragonal and orthorhombic phases is more subtle, but the shorter phonon lifetimes of the *Pnma* phase outweigh the slightly larger group velocities and κ_w to yield a 5–10% lower κ_{latt}.

More generally, the short phonon lifetimes in comparison to the chalcogenides suggests that the most fruitful approach to optimising the κ_{latt} of the oxide perovskites is likely to be targeting lower group velocities, *e.g.* through weaker or less homogeneous chemical bonding, the latter through structure types with larger/lower-symmetry unit cells. Our recent set of similar calculations on the $LnCoO_3$ identified lower group velocities, attributed to the weaker ionic bonding, as a key factor in the lower κ_{latt}, which lends support to this hypothesis.[79]

Finally, we also consider the directional anisotropy in the $\boldsymbol{\kappa}_{latt}$. Due to the symmetry of the *Pm*$\bar{3}$*m*, *I*4/*mcm* and *Pnma* structures, the equivalences of the diagonal elements of the $\boldsymbol{\kappa}_{latt}$ are $\kappa_{xx} = \kappa_{yy} = \kappa_{zz} = \kappa_{latt}$, $\kappa_{xx} = \kappa_{yy} \neq \kappa_{zz}$ and $\kappa_{xx} \neq \kappa_{yy} \neq \kappa_{zz}$. The independent components of the $\boldsymbol{\kappa}_p$, obtained using the SM-RTA and LBTE, the $\boldsymbol{\kappa}_w$ and the $\boldsymbol{\kappa}_{latt}$ at T = 1000 K are compared in Tables S3 and S4. The $\boldsymbol{\kappa}_p$ of the *I*4/*mcm* phase show modest anisotropy, with the thermal conductivity along the $a = b$ and c directions differing from the scalar average κ_p in Table 2 by 7.6 and 15% respectively, and with similar % differences obtained for both the SM-RTA and LBTE κ_p. The anisotropy in the *Pnma* phase is much smaller, at 2.1–4.4% of the κ_p. The anisotropy in the $\boldsymbol{\kappa}_w$ is also relatively small, with maximum differences of 2.8 and 4.1% in the orthorhombic and tetragonal phases. Notably, differences in the κ_p and $\boldsymbol{\kappa}_w$ combine to minimise the anisotropy in the $\boldsymbol{\kappa}_{latt}$, with differences of 2.9–6% and 1.4–4.1%, respectively, for the *I*4/*mcm* and *Pnma* phases. Our calculations therefore predict minimal anisotropy in the $\boldsymbol{\kappa}_{latt}$ in both non-cubic phases of STO.

As noted in the previous section, the $c = z$ and $b = y$ directions in the *I*4/*mcm* and *Pnma* phases are equivalent to the $a = b = c$ directions in the *Pm*$\bar{3}$*m* phase. For the tetragonal phase, we predict the largest κ_p along the c direction, and the κ_{latt} along this direction obtained using the SM-RTA and LBTE κ_p are equal to and 2.7% smaller than, respectively, the κ_{latt} along the three axes in the cubic phase. For the orthorhombic phase, on the other hand, we predict the lowest κ_p and κ_w along the b direction, with the result that the κ_{latt} is 14–19% smaller than in the cubic phase. This suggests that the phonon transport along the c direction in the *I*4/*mcm* phase remains similar to the parent cubic phase, but is significantly disrupted in the *Pnma* phase, which again highlights the large impact of the lower crystal symmetry on the κ_{latt}.

3.2 Electronic structure and transport properties

The electronic band structure and density of states (DoS) of the three $SrTiO_3$ phases are compared in Fig. 6. In all three systems,

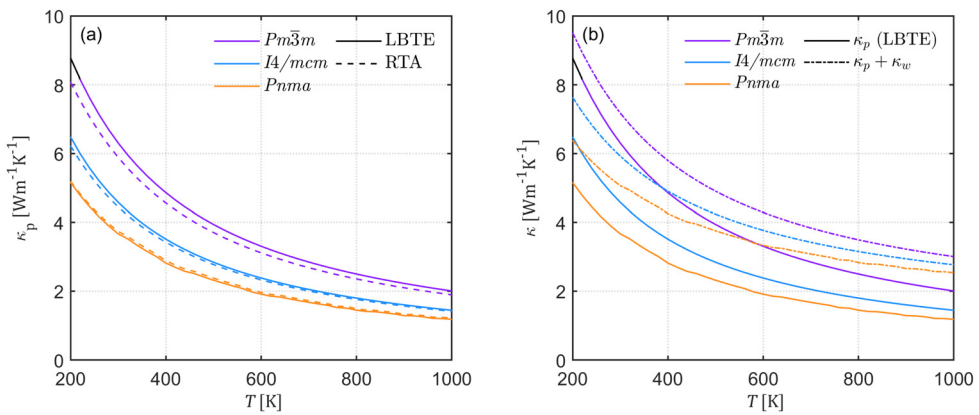

Fig. 5 Contribution to the scalar-average lattice thermal conductivity κ_{latt} of the *Pm*$\bar{3}$*m*, *I*4/*mcm* and *Pnma* phases of $SrTiO_3$ from "particle-like" (band) and "wave-like" (interband tunnelling) transport, κ_p/κ_c, as a function of temperature. Plot (a) compares the κ_p obtained with the single-mode relaxation-time approximation (eqn (2)) and by full solution of the linearised Boltzmann transport equation (LBTE).[50,52] Plot (b) compares the κ_p obtained by solving the LBTE and the total $\kappa_{latt} = \kappa_p + \kappa_w$ obtained by solving the Wigner transport equation to include interband tunnelling.[51]

Table 3 Calculated electronic band gaps E_g of the three phases of $SrTiO_3$ examined in this work compared to experimental studies

	$E_{g,dir}$ [eV]	$E_{g,indir}$ [eV]
$Pm\bar{3}m$	4.23	4.0
$I4/mcm$	4.15	4.14
$Pnma$	4.13	—
Expt[81,82]	3.75	3–3.25

the valence- and conduction-band edges are formed respectively from O 2p and Ti 3d states. The impact of crystal symmetry on the electronic band structure is similar to that on the phonon dispersion, with the increase in the complexity of the unit cells from the $Pm\bar{3}m$ to the $Pnma$ phase resulting in more complex band structures. In the $Pm\bar{3}m$ phase, the valence-band maximum (VBM) is located at $\boldsymbol{k} = R$, whereas in the $I4/mcm$ and $Pnma$ phases the VBM is located along the $\Gamma \rightarrow X$ and $\Gamma \rightarrow W$ paths, respectively. The conduction-band minimum (CBM) of all three phases is located at $\boldsymbol{k} = \Gamma$.

Using the HSE06 hybrid functional, we predict bandgaps E_g between 4–4.25 eV for the three phases (Table 3), which are considerably larger than both the direct E_g = 3–3.25 eV and the indirect E_g = 3.75 eV reported in experiments.[81,82] However, given the large E_g we would not expect the overestimation of the bandgaps to significantly impact the calculated electronic properties. A measured bandgap for $Pnma$ STO is not available, but our predicted band gap value is consistent with the insulating nature predicted in ref. 83.

Fig. 7 shows the predicted scalar-average electrical conductivity σ, absolute Seebeck coefficient $|S|$, power factor $S^2\sigma$ (PF) and electronic thermal conductivity κ_{el} of the three STO phases with n-type doping as a function of doping level n at a fixed T = 1000 K. A similar plot showing the temperature dependence of the properties at a fixed $n = 2 \times 10^{21}$ cm^{-3} is provided in Fig. S2.

The relationship between n and σ is given by:

$$\sigma = \frac{ne^2\tau^{el}}{m_\sigma^*} \tag{28}$$

τ^{el} is a weighted-average electron lifetime, comparable to the τ^{ph} obtained from analysing the particle-like lattice thermal conductivity (*cf.* eqn (19)). Similarly, m_σ^* is a weighted-average carrier effective mass for electronic conductivity, averaged over the bands that contribute to the σ. The approximately linear rise in σ with n results in a steep rise in σ when the carrier concentration is plotted on a logarithmic scale as in Fig. 7(a). We predict that $n > 10^{20}$ cm^{-3} are required to obtain a reasonable $\sigma \approx$ 10s of S cm^{-1}.

On the other hand, the S is inversely proportional to the n according to:

$$S = \frac{8\pi^2 k_B^2}{3qh^2} m_S^* \left(\frac{\pi}{3n}\right)^{2/3} \tag{29}$$

where $q = \pm e$ for hole and electron carriers and m_S^* is the Seebeck effective mass, which is related to m_σ^* through:[11]

$$m_S^* = N_V^{2/3} m_\sigma^* \tag{30}$$

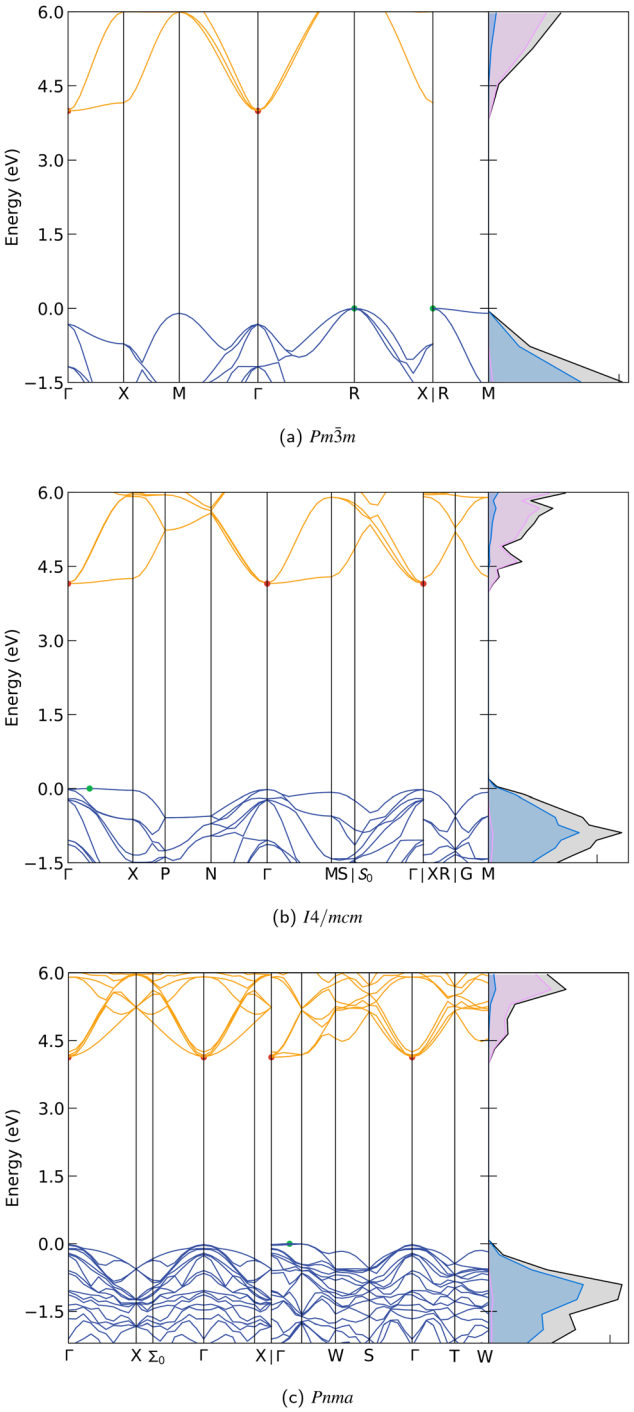

Fig. 6 Electronic band structure and density of states (DoS) of $Pm\bar{3}m$ (a), $I4/mcm$ (b) and $Pnma$ $SrTiO_3$ (c). On each band structure the valence and conduction bands are coloured blue and yellow, respectively, and the valence- and conduction-band minima are marked by green and red circles. On each DoS plot, the total DoS is shown in grey and the projections onto the O 2p and Ti 3d states are shown in blue and pink, respectively.

where N_V is the valley degeneracy. This dependence results in a monotonic decrease in $|S|$ with n when the carrier concentration is plotted on a logarithmic scale (Fig. 7(b)).

The opposing behaviour of σ and $|S|$ result in a peak in the $S^2\sigma$, with the PFs optimised at $n \approx 2 \times 10^{21}$ cm^{-3}. This is in line

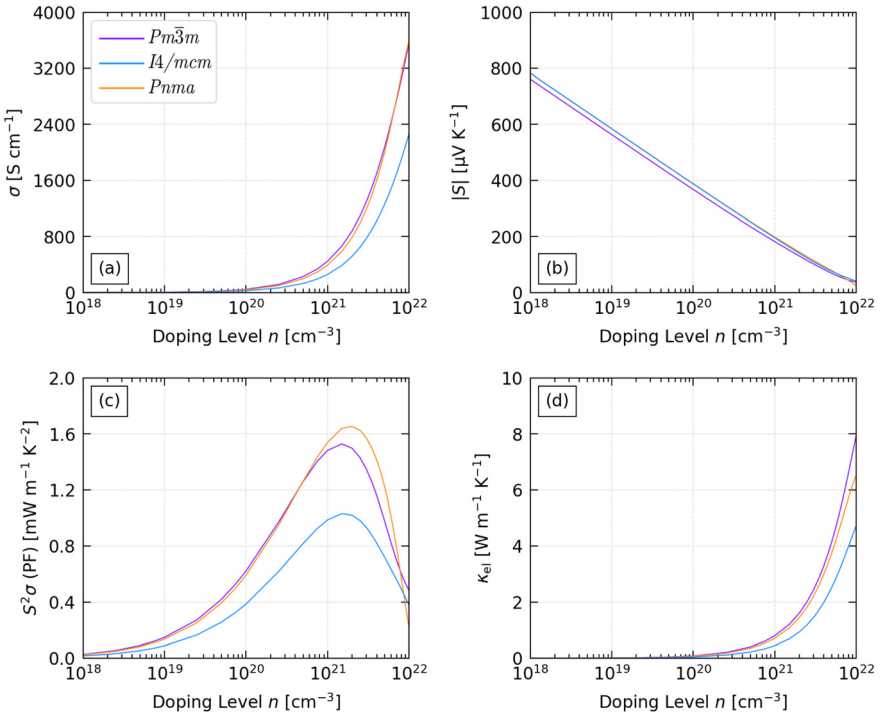

Fig. 7 Predicted scalar-average electrical properties of n-type $Pm\bar{3}m$, $I4/mcm$ and $Pnma$ $SrTiO_3$ as a function of extrinsic carrier concentration n ("doping level") at a fixed temperature T = 1000 K: (a) electrical conductivity σ, (b) absolute Seebeck coefficient $|S|$, (c) power factor $S^2\sigma$ (PF), and (d) electronic thermal conductivity κ_{el}.

with previous studies.[43,84] While pristine stoichiometric $SrTiO_3$ can have relatively low n on the order of 10^{15} cm^{-3},[85] exposure of the material to reducing conditions can produce high concentrations of oxygen vacancies, which act as electron donors, and yield carrier concentrations above 10^{20} cm^{-3} without explicit chemical doping.[86] It is possible to obtain $n > 10^{21}$ cm^{-3} with explicit doping, for example by replacing Sr with La and/or Ti with Nb.[86–88] The carrier concentration we predict is required to optimise the PFs should therefore be readily accessible in experiments.

Finally, large n results in "degenerate" semiconducting behaviour with a metallic-like dependence of the conductivity on temperature (Fig. S2). Under these circumstances, the κ_{el} is related to the σ through the Wiedemann–Franz law:

$$\kappa_{el} = L\sigma T \quad (31)$$

where L is the Lorentz number. As a result, the κ_{el} rises steeply above $n \approx 10^{20}$ cm^{-3}, reaching values of $\sim$1 W m^{-1} K^{-1} at the $n \approx 2 \times 10^{21}$ cm^{-3} that optimises the PF, and becomes comparable in magnitude to the κ_{latt} at $n \approx 5 \times 10^{21}$ cm^{-3} (Fig. 7(d), *cf.* Table 2).

We note that we have excluded the temperature dependence of the properties in eqn (28)–(31) for brevity, but the effective masses m^*_σ/m^*_S, τ^{el} and L are in general temperature dependent. All four parameters also in general depend on the n.

Table 4 lists the values of the four electrical properties at $n = 2 \times 10^{21}$ cm^{-3} and T = 1000 K. We predict the $Pm\bar{3}m$ and $Pnma$ phases to show similar electrical properties, with the former having a 10% higher σ and the latter an 11% larger $|S|$. The net result is that the $Pnma$ phase is predicted to have a 10% larger PF and, due to its lower σ, a 10% lower κ_{el}. On the other hand, while all three phases have similar $|S|$, the $I4/mcm$ phase has notably lower σ, which results in a 32/62% smaller peak PF compared to the $Pm\bar{3}m$ and $Pnma$ phases, albeit with the benefit of a 40–60% lower κ_{el}.

Given the similar band structure and E_g, the lower electrical conductivity of the $I4/mcm$ phase is somewhat surprising. To investigate this further, we followed the procedure in ref. 89 to obtain an estimate of the m^*_σ and m^*_S. This entails performing calculations using the constant relaxation-time approximation

Table 4 Analysis of the scalar-average n-type electronic properties of the three phases of $SrTiO_3$ examined in this work at T = 1000 K and $n = 2 \times 10^{21}$ cm^{-3}. For each phase we show the electronic conductivity σ, Seebeck coefficient S, power factor $S^2\sigma$ and electronic thermal conductivity κ_{el}. We also show the conductivity and Seebeck effective masses m^*_σ/m^*_S and weighted-average electronic lifetime τ^{el} calculated as described in the text

	σ [S cm^{-1}]	S [μV K^{-1}]	$S^2\sigma$ [mW m^{-1} K^{-2}]	κ_{el} [W m^{-1} K^{-1}]	m^*_σ [m_e]	m^*_S [m_e]	τ_{el} [fs]
$Pm\bar{3}m$	88.1	−130	1.5	1.61	0.78	2.21	1.22
$I4/mcm$	51.9	−140	1.02	0.93	0.82	2.34	0.76
$Pnma$	78.9	−145	1.65	1.45	0.8	2.4	1.12

(CRTA), in which the $\tau_{\boldsymbol{k}j}$ in eqn (9) are replaced by a constant relaxation time τ^{el}. In these calculations, the τ^{el} act as a scaling factor for the σ (*cf.* eqn (28)), and the CRTA conductivity and the σ calculated with per-state scattering rates can thus be used to determine weighted-average τ^{el} for comparing between systems in the same way as the τ^{ph} in eqn (19).

The calculated m^*_σ, m^*_S and τ^{el} at $n = 2 \times 10^{21}$ cm^{-3} and $T = 1000$ K are included in Table 4. We calculate very similar $m^*_\sigma = 0.74{-}0.79\ m_{\mathrm{e}}$ and $m^*_S = 2.29{-}2.49\ m_{\mathrm{e}}$ for the three systems. The 5.9 and 8.6% larger m^*_S of the *I*4/*mcm* and *Pnma* phases compared to the cubic phase account for the majority of the 7.7/11.5% larger $|S|$. On the other hand, the 2.6–5.1% difference in the m^*_σ of the *Pnma* and *I*4/*mcm* phases compared to the *Pm*$\bar{3}$*m* phase indicate that the much lower σ of the tetragonal phase is not due to differences in the carrier effective masses. Instead, the calculated τ^{el} indicate that the *I*4/*mcm* phase has significantly stronger electron scattering compared to the other two phases.

Analysis of the mobility μ as a function of n at $T = 1000$ K shows that the μ is dominated by polar-optic phonon (POP) scattering (Fig. S3). The associated μ_{POP} are between 1.5–2× larger in the *Pnma* and *Pm*$\bar{3}$*m* phases, indicating that the shorter τ^{el} in the *I*4/*mcm* phase is due to stronger POP scattering. The treatment of POP scattering in this work is based on the Frölich model for an electron in a dielectric medium interacting with a dispersionless optic phonon mode with frequency ω_{po}.[90] The scattering matrix elements g are of the form:[91]

$$g \propto \left[\frac{\hbar\omega_{\mathrm{po}}}{2}\left(\frac{1}{\varepsilon_\infty} - \frac{1}{\varepsilon_{\mathrm{S}}}\right)\right]^{\frac{1}{2}} \tag{32}$$

where ε_∞ and ε_{S} are the scalar averages of the high-frequency and static dielectric constants. The three systems have similar ω_{po} = 5.2–6.5 THz and similar ε_∞ = 6.75–7 ε_0. The ε_{S} span a much larger range of 220–350 ε_0 but are larger than the ε_∞, so the latter dominate the right-hand expression in eqn (32). AMSET uses a modified version of the Frölich model that accounts for anisotropy in the dielectric properties, but this is unlikely to explain the stronger POP scattering in the *I*4/*mcm* phase because the $\boldsymbol{\varepsilon}_\infty$ tensors of all three phases are almost isotropic, with the directional components $\varepsilon_{\infty,\alpha\alpha}$ differing by at most 2% from the scalar averages. The matrix elements in AMSET also incorporate a term for the overlap of the electronic states. Moreover, to calculate the scatteing rates (inverse lifetimes), the g are combined with an expression accounting for thermal population and the conservation of energy similar to those in eqn (23) and (24).[54] It is currently not possible to separate these two types of contribution from the "nature" of the electronic states, but we can nonetheless infer that the stronger POP scattering in the *I*4/*mcm* phase is due to either or both of these and not to differences in the model optic phonon and dielectric properties.

We recently performed a similar analysis for the chalcogenides SnS and SnSe,[80] which yielded m^*_σ and $m^*_S = 0.15{-}0.27$ and 0.7–0.81 respectively. The oxides have a larger m^*_σ, resulting in lower σ that requires roughly an order of magnitude larger n to offset. While the oxides have a 3–4× larger m_{S}, potentially resulting in a larger $|S|$, this is counterbalanced by the large n required to optimise the PF. Also, while ref. 80 did not calculate τ^{el}, similar results to those obtained with per-state $\tau_{\boldsymbol{k}j}$ were obtained using a typical τ^{el} = 10 fs (10^{-14} s), which suggests a weighted-average relaxation time around an order of magnitude longer than we calculate for STO. The analysis of the κ_{latt} in the previous section suggested that the stronger bonding in the oxides may lead to stronger phonon anharmonicity and shorter phonon lifetimes. Drawing a parallel, analysis of the τ^{el} suggests that this also results in stronger electron scattering and shorter electron lifetimes.

Our previous study of the $LnCoO_3$ yielded $m^*_\sigma = 2.26{-}2.6\ m_{\mathrm{e}}$ and $m^*_S = 5.27{-}5.74\ m_{\mathrm{e}}$ at the n that maximise the PF.[79] In terms of optimising the properties, this suggests that, as for the κ_{latt}, exploring alternative perovskite chemistries may be fruitful, although weaker chemical bonding may have the undesirable side effect of increasing the conductivity effective masses. It would be of particular interest to determine whether the much lower σ of the *I*4/*mcm* phase is replicated over other perovskite materials, as, if so, it would imply that this phase should ideally be avoided. The results in the present study are however insufficient to confirm, or otherwise, the generality of this finding.

Finally, we again consider the directional anisotropy in the electrical properties. The diagonal $\sigma_{\alpha\alpha}$, $S_{\alpha\alpha}$ and $\kappa_{\mathrm{el},\alpha\alpha}$ components of the $\boldsymbol{\sigma}$, $\boldsymbol{S}$ and $\boldsymbol{\kappa}_{\mathrm{el}}$ tensors, and the corresponding power factors ${S_{\alpha\alpha}}^2\sigma_{\alpha\alpha}$, calculated at $n = 2 \times 10^{21}$ cm^{-3} and $T = 1000$ K are shown in Table S5. The tetragonal phase shows fairly minimal anisotropy, with up to 5% differences in the directional σ, S and $S^2\sigma$ compared to the scalar averages, and a slightly larger 7.5% variation in the κ_{el}. The electrical properties of the orthorhombic phase show more anisotropy, with up to 6–9% variation in the σ, S and κ_{el}, and 12.7/10.9% higher/lower $S^2\sigma$ along the crystallographic b and c directions compared to the scalar average, which, for this system, is close to the PF along the a direction. While larger than the anisotropy in the $\boldsymbol{\kappa}_{\mathrm{latt}}$, we still consider this to be relatively modest.

The *I*4/*mcm* structure shows the largest σ and κ_{el} but the smallest $|S|$ along the c direction. The $|S|$ is similar to the cubic phase, but the σ and κ_{el} are much smaller, as is the $S^2\sigma$. The equivalent comparison for the *Pnma* phase shows the smallest σ, largest $|S|$ and intermediate κ_{el} along the b direction. The σ and κ_{el} are lower than those in the *Pm*$\bar{3}$*m* phase, but more comparable than those in the tetragonal phase, whereas the $|S|$ and, consequently, the PF, are significantly larger. We therefore infer that the distortions in the two lower-symmetry phases have a significant impact on the electrical properties relative to the cubic phase, even when compared along equivalent directions.

3.3 Thermoelectric figure of merit

Combining the lattice thermal conductivity and electrical-transport properties discussed in the two preceding sections allows us to predict the figure of merit zT. Our analysis of the κ_{latt} found that the additional contribution to the "particle-like" conductivity, κ_{p}, obtained by solving the linearised Boltzmann transport equation over the less computationally-demanding

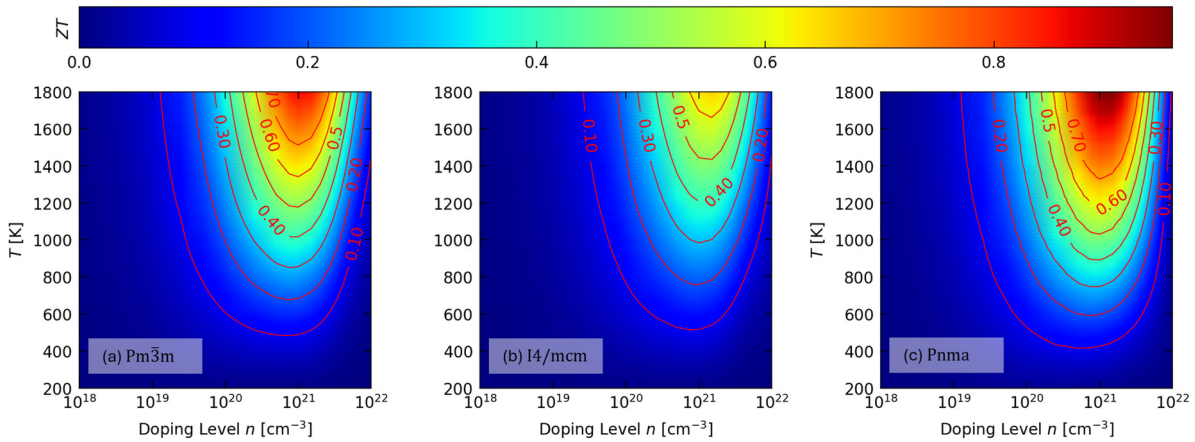

Fig. 8 Predicted scalar-average n-type thermoelectric figure of merit zT of $Pm\bar{3}m$ (a), $I4/mcm$ (b) and $Pnma$ $SrTiO_3$ (c) as a function of extrinsic carrier concentration ("doping level") n and temperature T.

single-mode relaxation-time approximation was relatively small, but that the wave-like contribution from interband tunnelling, κ_w, was significant in all three phases. On the basis that combining the LBTE κ_p with the κ_w should give the most accurate description of the κ_{latt}, we used these values for calculating the zT.

Fig. 8 shows the predicted scalar-average zT of the three phases of $SrTiO_3$ as a function of doping level n and temperature T. Given the fall in the κ_{latt} with temperature and the behaviour of the power factor $S^2\sigma$ with n (*cf.* Fig. 5 and 7), the best performance is obtained at high T and relatively large $n \approx 10^{21}$ cm^{-3}.

Table 5 lists the maximum predicted zT, zT_{max}, at T = 400, 600 and 1000 K, roughly matching the low-, mid- and high-temperature heat-recovery scenarios outlined in ref. 92. We predict zT_{max} of <0.1, 0.13–0.21 and 0.31–0.47 at the three temperatures, all of which are lower than the typical benchmark zT = 1 but which are consistent at the higher temperature with experimental measurements. With the exception of the cubic and tetragonal phases having similar predicted zT_{max} at 400 K, we predict that the zT fall in the order of $Pnma > Pm\bar{3}m > I4/mcm$ at all three temperatures. The relatively poor performance of the tetragonal phase is primarily due to its low conductivity, which does not compensate for its larger absolute Seebeck coefficient and results in a low power factor. On the other hand, the superior performance of the $Pnma$ phase compared to the $Pm\bar{3}m$ phase is primarily due to its 15–30% lower κ_{latt} and correspondingly lower total thermal conductivity, as well as to the combination of slightly lower σ and slightly larger $|S|$ producing a 2–4% larger $S^2\sigma$.

Table S6 compares the directional values of the zT, $S^2\sigma$ and κ_{tot} under the same conditions as the zT_{max} in Table 5. The zT of the $I4/mcm$ phase show modest anisotropy, with a 3.2% larger zT_{max} along the $a = b$ directions and a 6.5% smaller zT_{max} along the c direction compared to the scalar average at T = 1000 K. This is due primarily to differences in the thermal conductivity. The $Pnma$ phase shows more significant anisotropy, with a 3.9% larger PF and 4.3% smaller κ_{tot} along the b direction resulting in an 8.4% higher zT_{max} compared to the scalar average, and a 7.8% smaller PF and 0.93% higher κ_{tot} along the c direction producing a 10% lower zT_{max}. As for the electrical properties, we find little correspondence between the zT of the cubic phase and the zT along the c direction in the $I4/mcm$ phase and the b

Table 5 Predicted maximum scalar-average n-type zT, zT_{max}, of the three phases of $SrTiO_3$ examined in this work at T = 400, 600 and 1000 K, roughly corresponding to the low-, medium- and high-temperature heat-recovery scenarios outlined in ref. 92. For each predicted zT we also show the associated extrinsic carrier concentrations ("doping levels") n, Seebeck coefficients S, electrical conductivities σ, power factors $S^2\sigma$ (PFs), and lattice, electronic and total thermal conductivities κ_{latt}, κ_{el} and κ_{tot}

							κ [W m^{-1} K^{-1}]		
	T [K]	n [cm^{-3}]	zT	S [μV K^{-1}]	σ [S cm^{-1}]	$S^2\sigma$ (PF) [mW m^{-1} K^{-2}]	κ_{el}	κ_{latt}	κ_{tot}
$Pm\bar{3}m$	400	7.5×10^{20}	0.06	−109	900	1.06	0.76	5.79	6.55
	600	7.5×10^{20}	0.15	−150	581	1.31	0.7	4.29	4.99
	1000	1×10^{21}	0.39	−182	448	1.48	0.79	3.01	3.8
$I4/mcm$	400	7.5×10^{20}	0.06	−128	484	0.79	0.4	4.9	5.3
	600	1×10^{21}	0.13	−148	432	0.94	0.49	3.77	4.26
	1000	1×10^{21}	0.31	−195	261	0.99	0.45	2.77	3.22
$Pnma$	400	5×10^{20}	0.09	−148	500	1.08	0.4	4.25	4.65
	600	7.5×10^{20}	0.21	−166	487	1.34	0.58	3.33	3.91
	1000	1×10^{21}	0.47	−198	392	1.54	0.7	2.54	3.24

direction in the *Pnma* phase, which indicates that the large impact of the structural distortions on the electrical properties also carries through to the figure of merit.

Experimental values of zT span a range of 0.27–0.37, with σ = 200–303 S cm^{-1}, S = −168 to −233 μV K^{-1}, and κ = 2.6–3.1 W m^{-1} K^{-1} at T = 1000 K.[93–95] Assuming the $Pm\bar{3}m$ phase, we predict values of between zT = 0.2 (n = 10^{20} cm^{-3}, σ = 46.1 S cm^{-1}, S = −367 μV K^{-1}, κ = 3.09 W m^{-1} K^{-1}) and zT = 0.37 (n = 5 × 10^{20} cm^{-3}, σ = 227 S cm^{-1}, S = −152 μV K^{-1}, κ = 3.41 W m^{-1} K^{-1}). These predictions, in particular those at the larger n, are reasonably consistent with experimental measurements, confirming the accuracy of our modelling approach. In particular, with reference to Table 2, and as found in our previous work,[79] accounting for wave-like tunnelling contributions to the κ_{latt} results in a notably better match to experiments. With this in mind, our predictions suggest that experiments have likely achieved close to the maximum possible for pristine bulk-like cubic STO, but that significant performance enhancements could be possible by targeting chemical modifications (*e.g.* doping) that stabilise the orthorhombic phase – according to our analysis, doing so would largely retain the favourable electrical properties of the $Pm\bar{3}m$ phase while significantly reducing the κ_{latt}.

4 Conclusions

In summary, we have carried out a detailed *ab initio* modelling study of the impact of crystal structure on the thermoelectric performance of the archetypal oxide perovskite $SrTiO_3$ in the orthorhombic *Pnma*, tetragonal *I*4/*mcm* and cubic $Pm\bar{3}m$ phases.

Analysis of the structural dynamics and lattice thermal conductivity shows that the primary impact of structure type is that the smaller primitive cell of the $Pm\bar{3}m$ phase results in larger phonon group velocities and a larger contribution from ''particle-like'' (band) transport to the κ_{latt}, which more than offsets its shorter phonon lifetimes. More generally, compared to the flagship Group IV–VI chalcogenide thermoelectrics the oxides show relatively strong phonon scattering and short phonon lifetimes, but this is more than compensated by larger group velocities. Based on this, efforts to optimise (*i.e.* reduce) the κ_{latt} of STO and other oxide perovskites should focus on chemical modifications or alternative perovskite chemistries that favour lower-symmetry crystal structures and/or which have weaker/less homogeneous chemical bonding. A second notable finding from our analysis of the κ_{latt} is the contribution from wave-like transport, which has a large impact on all three phases but is most significant for the lower-symmetry structures. Taken together with our previous work on the lanthanide cobalates, we suggest that accounting for transport through this mechanism is important for an accurate description of the κ_{latt} in oxide perovskites generally, and that the increase in this term in lower-symmetry structures may be universal across different oxide perovskite chemistries.

Analysis of the electrical properties indicates that the *I*4/*mcm* phase has significantly lower electrical conductivity due to strong polar-optic phonon scattering, whereas the *Pnma* phase shows comparable or higher power factors to the cubic $Pm\bar{3}m$ phase due to the combination of a lower σ and larger absolute Seebeck coefficient. Comparing again to the Group IV–VI chalcogenides, we find that the power factors of the oxides are limited by high conductivity effective masses and short electron lifetimes, and that the high carrier concentrations required to offset this effectively nullify the higher $|S|$. From a fundamental perspective, it is interesting to note that the oxides show both short phonon and electron lifetimes, which could indicate that the electrical properties and κ_{latt} may be coupled in a way which is yet to be explored in detail. We also believe the low predicted σ of the *I*4/*mcm* phase warrants further investigation, particularly to determine whether similar behaviour is observed across different perovskite chemistries.

Finally, our predicted zT show that, while STO cannot achieve the benchmark $zT \geq 1$ even at a high T = 1000 K, it may be possible to significantly improve upon existing experimental studies by targeting the stabilisation of lower-symmetry structures and in particular the orthorhombic *Pnma* phase.

We hope that the results presented here will ultimately provide some important insight to support ongoing efforts to obtain high-performance oxide thermoelectrics for sustainable energy recovery.

Author contributions

Conceptualization, methodology, software and writing – all authors; data curation, formal analysis and investigation – AZK and JMF; funding acquisition – JMS; project administration and supervision – JMF and JMS; resources – JMS.

Conflicts of interest

There are no conflicts to declare.

Data availability

Supplementary information: Optimised lattice parameters and comparison to experimental measurements; analysis of the ''particle-like'' contributions to the lattice thermal conductivity at 300 K; anisotropy in the κ_{latt} at 1000 K; ''scattering phase space''; functions for the *I*4/*mcm* and *Pnma* phases of $SrTiO_3$; anisotropy in the electrical transport at 1000 K; analysis of the electron mobility as a function of carrier concentration at 1000 K; and anisotropy in the thermoelectric figure of merit at 400, 600 and 1000 K. See DOI: **https://doi.org/10.1039/d5ya00105f**.

Raw data from this study will be made available to download free of charge after publication from an online repository at **https://doi.org/10.17632/9h4b89b79r**. Our analysis code is available on GitHub at **https://github.com/skelton-group/ZT-Calc-Workflow**.

Acknowledgements

AZK is supported by a University of Manchester PhD studentship, and JMF and JMS are supported by a UK Research and

Innovation (UKRI) Future Leaders Fellowship (MR/T043121/1, MR/Y033973/1). The calculations used the ARCHER 2 HPC facility *via* the UK Materials Chemistry Consortium, which is funded by the UK Engineering and Physical Sciences Research Council (EP/R029431, EP/X035859).

Notes and references

1 World Meteorological Organization, *State of the Climate Report*, 2024.
2 H. Ritchie and M. Roser, *CO_2 and Greenhouse Gas Emissions*, 2020, **https://ourworldindata.org/emissions-by-sector**.
3 I. MacLeay, K. Harris and A. Annut, *Digest of united kingdom energy statistics 2015*, Stationery Office, in Department of Energy & Climate Change National Statistics, 2015.
4 R. Freer and A. V. Powell, *J. Mater. Chem. C*, 2020, **8**, 441–463.
5 H. Xie, Y. Zhang and P. Gao, *Micromachines*, 2023, **14**, 31.
6 T. Torfs, V. Leonov, C. V. Hoof and B. Gyselinckx, *2006 5th IEEE Conference on Sensors*, 2006, pp. 427–430.
7 Y. Rao, C. Xu, M. Voss, P. Ying, H. Reith, K. Nielsch, T. Bechtold and D. Hohlfeld, *Adv. Mater. Technol.*, 2024, **9**, 2301157.
8 N. V. Burnete, F. Mariasiu, C. Depcik, I. Barabas and D. Moldovanu, *Prog. Energy Combust. Sci.*, 2022, **91**, 101009.
9 H. Zhou, T. Tian, X. Wang and J. Li, *Appl. Energy*, 2023, **332**, 120539.
10 L. Catalan, P. Alegria, M. Araiz and D. Astrain, *Appl. Therm. Eng.*, 2023, **222**, 119843.
11 G. Tan, L.-D. Zhao and M. G. Kanatzidis, *Chem. Rev.*, 2016, **116**, 12123–12149.
12 A. Walsh, D. J. Payne, R. G. Egdell and G. W. Watson, *Chem. Soc. Rev.*, 2011, **40**, 4455–4463.
13 S. K. Guillemot, A. Suwardi, N. Kaltsoyannis and J. M. Skelton, *J. Mater. Chem. A*, 2024, **12**, 2932–2948.
14 R. Deng, X. Su, Z. Zheng, W. Liu, Y. Yan, Q. Zhang, V. P. Dravid, C. Uher, M. G. Kanatzidis and X. Tang, *Sci. Adv.*, 2018, **4**, eaar5606.
15 H. Lee, T. Kim, S. C. Son, J. Kim, D. Kim, J. Lee and I. Chung, *Mater. Today Phys.*, 2023, **31**, 100986.
16 B. Zhu, X. Liu, Q. Wang, Y. Qiu, Z. Shu, Z. Guo, Y. Tong, J. Cui, M. Gu and J. He, *Energy Environ. Sci.*, 2020, **13**, 2106–2114.
17 K. Biswas, J. He, I. D. Blum, C.-I. Wu, T. P. Hogan, D. N. Seidman, V. P. Dravid and M. G. Kanatzidis, *Nature*, 2012, **489**, 414–418.
18 Z. M. Gibbs, H. Kim, H. Wang, R. L. White, F. Drymiotis, M. Kaviany and G. Jeffrey Snyder, *Appl. Phys. Lett.*, 2013, **103**, 262109.
19 O. Delaire, J. Ma, K. Marty, A. F. May, M. A. McGuire, M.-H. Du, D. J. Singh, A. Podlesnyak, G. Ehlers, M. D. Lumsden and B. C. Sales, *Nat. Mater.*, 2011, **10**, 614–619.
20 D. Champier, *Energy Convers. Manage.*, 2017, **140**, 167–181.
21 I. Terasaki, *Phys. Rev. B: Condens. Matter Mater. Phys.*, 1997, **56**, 685–687.
22 H. Yakabe, K. Kikuchi, I. Terasaki, Y. Sasago and K. Uchinokura, *Proceedings of the 1997 16th International Conference on Thermoelectrics*, 1997, pp. 523–527.
23 W. Koshibae, K. Tsutsui and S. Maekawa, *Phys. Rev. B: Condens. Matter Mater. Phys.*, 2000, **62**, 6869–6872.
24 Y. Miyazaki, *Solid State Ionics*, 2004, **172**, 463–467.
25 M. Shikano and R. Funahashi, *Appl. Phys. Lett.*, 2003, **82**, 1851–1853.
26 H. Fukutomi, Y. Konno, K. Okayasu, M. Hasegawa and H. Nakatsugawa, *Mater. Sci. Eng., A*, 2009, **527**, 61–64.
27 J. D. Baran, M. Molinari, N. Kulwongwit, F. Azough, R. Freer, D. Kepaptsoglou, Q. M. Ramasse and S. C. Parker, *J. Phys. Chem. C*, 2015, **119**, 21818–21827.
28 R. Funahashi, I. Matsubara and S. Sodeoka, *Appl. Phys. Lett.*, 2000, **76**, 2385–2387.
29 J. Diez, E. Guilmeau, M. Madre, S. Marinel, S. Lemonnier and A. Sotelo, *Solid State Ionics*, 2009, **180**, 827–830.
30 E. Combe, R. Funahashi, T. Barbier, F. Azough and R. Freer, *J. Mater. Res.*, 2016, **31**, 1296–1305.
31 T. Tsubota, M. Ohtaki, K. Eguchi and H. Arai, *J. Mater. Chem.*, 1997, **7**, 85–90.
32 T. Okuda, K. Nakanishi, S. Miyasaka and Y. Tokura, *Phys. Rev. B: Condens. Matter Mater. Phys.*, 2001, **63**, 113104.
33 H. Muta, K. Kurosaki and S. Yamanaka, *J. Alloys Compd.*, 2003, **350**, 292–295.
34 H. Muta, K. Kurosaki and S. Yamanaka, *J. Alloys Compd.*, 2005, **392**, 306–309.
35 T. Kobayashi, H. Takizawa, T. Endo, T. Sato, M. Shimada, H. Taguchi and M. Nagao, *J. Solid State Chem.*, 1991, **92**, 116–129.
36 D. Flahaut, T. Mihara, R. Funahashi, N. Nabeshima, K. Lee, H. Ohta and K. Koumoto, *J. Appl. Phys.*, 2006, **100**, 084911.
37 D. A. Muller, N. Nakagawa, A. Ohtomo, J. L. Grazul and H. Y. Hwang, *Nature*, 2004, **430**, 657–661.
38 J. Haeni, P. Irvin, W. Chang, R. Uecker, P. Reiche, Y. Li, S. Choudhury, W. Tian, M. Hawley, B. Craigo, A. Tagantsev, X. Pan, S. Streiffer, L. Chen, S. Kirchoefer, J. Levy and D. Schlom, *Nature*, 2004, **430**, 758–761.
39 H. Muta, A. Ieda, K. Kurosaki and S. Yamanaka, *Mater. Lett.*, 2004, **58**, 3868–3871.
40 A. F. Santander-Syro, O. Copie, T. Kondo, F. Fortuna, S. Pailhès, R. Weht, X. G. Qiu, F. Bertran, A. Nicolaou, A. Taleb-Ibrahimi, P. Le Fèvre, G. Herranz, M. Bibes, N. Reyren, Y. Apertet, P. Lecoeur, A. Barthélémy and M. J. Rozenberg, *Nature*, 2011, **469**, 189–193.
41 C. Mallada, J. Menéndez, O. Dura, M. López de la Torre, R. Menéndez and R. Santamaría, *J. Eur. Ceram. Soc.*, 2017, **37**, 3741–3746.
42 A. Mubarak, *Int. J. Mod. Phys. B*, 2016, **30**, 1650141.
43 A. Z. Khan, J. M. Flitcroft and J. M. Skelton, *Mater. Adv.*, 2024, **5**, 652–664.
44 S. Kumar, A. Barasheed and H. Alshareef, *ACS Appl. Mater. Interfaces*, 2013, **5**, 7268–7273.
45 L. Goncalves, P. Alpuim, A. Rolo and J. Correia, *Thin Solid Films*, 2011, **519**, 4152–4157.
46 S. Saini, P. Mele and A. Tiwari, *J. Phys. Chem. Solids*, 2019, **129**, 347–353.
47 W. Zhao, S. Fan, N. Xiao, D. Liu, Y. Tay, C. Yu, D. Sim, H. Hng, Q. Zhang, F. Boey, J. Ma, X. Zhao, H. Zhang and Q. Yan, *Energy Environ. Sci.*, 2012, **5**, 5364–5369.

48 J. Chen, H. Chen, F. Hao, X. Ke, N. Chen, T. Yajima, Y. Jiang, X. Shi, K. Zhou, M. Döbeli, T. Zhang, B. Ge, H. Dong, H. Zeng, W. Wu and L. Chen, *ACS Energy Lett.*, 2017, **2**, 915–921.
49 S. Ohta, T. Nomura, H. Ohta and K. Koumoto, *J. Appl. Phys.*, 2005, **97**, 034106.
50 A. Togo, L. Chaput and I. Tanaka, *Phys. Rev. B: Condens. Matter Mater. Phys.*, 2015, **91**, 094306.
51 M. Simoncelli, N. Marzari and F. Mauri, *Phys. Rev. X*, 2022, **12**, 041011.
52 L. Chaput, *Phys. Rev. Lett.*, 2013, **110**, 265506.
53 G. K. Madsen, J. Carrete and M. J. Verstraete, *Comput. Phys. Commun.*, 2018, **231**, 140–145.
54 A. M. Ganose, J. Park, A. Faghaninia, R. Woods-Robinson, K. A. Persson and A. Jain, *Nat. Commun.*, 2021, **12**, 2222.
55 G. Kresse and J. Hafner, *Phys. Rev. B: Condens. Matter Mater. Phys.*, 1993, **47**, 558–561.
56 A. Jain, S. P. Ong, G. Hautier, W. Chen, W. D. Richards, S. Dacek, S. Cholia, D. Gunter, D. Skinner, G. Ceder and K. A. Persson, *APL Mater.*, 2013, **1**, 011002.
57 J. P. Perdew, A. Ruzsinszky, G. I. Csonka, O. A. Vydrov, G. E. Scuseria, L. A. Constantin, X. Zhou and K. Burke, *Phys. Rev. Lett.*, 2008, **100**, 136406.
58 P. E. Blöchl, *Phys. Rev. B: Condens. Matter Mater. Phys.*, 1994, **50**, 17953–17979.
59 G. Kresse and D. Joubert, *Phys. Rev. B: Condens. Matter Mater. Phys.*, 1999, **59**, 1758–1775.
60 H. J. Monkhorst and J. D. Pack, *Phys. Rev. B: Condens. Matter Mater. Phys.*, 1976, **13**, 5188–5192.
61 A. Togo and I. Tanaka, *Scr. Mater.*, 2015, **108**, 1–5.
62 X. Gonze and C. Lee, *Phys. Rev. B: Condens. Matter Mater. Phys.*, 1997, **55**, 10355–10368.
63 M. Gajdoš, K. Hummer, G. Kresse, J. Furthmüller and F. Bechstedt, *Phys. Rev. B: Condens. Matter Mater. Phys.*, 2006, **73**, 045112.
64 A. V. Krukau, O. A. Vydrov, A. F. Izmaylov and G. E. Scuseria, *J. Chem. Phys.*, 2006, **125**, 224106.
65 J. M. Skelton, D. S. D. Gunn, S. Metz and S. C. Parker, *J. Chem. Theory Comput.*, 2020, **16**, 3543–3557.
66 A. M. Ganose, A. J. Jackson and D. O. Scanlon, *J. Open Source Software*, 2018, **3**, 717.
67 D. Porezag and M. R. Pederson, *Phys. Rev. B: Condens. Matter Mater. Phys.*, 1996, **54**, 7830–7836.
68 J. M. Skelton, L. A. Burton, A. J. Jackson, F. Oba, S. C. Parker and A. Walsh, *Phys. Chem. Chem. Phys.*, 2017, **19**, 12452–12465.
69 X. Wu, D. Vanderbilt and D. M. Hamann, *Phys. Rev. B*, 2005, **72**, 035105.
70 R. Shukla, S. J. Patwe, S. K. Deshpande, S. N. Achary, P. S. R. Krishna, A. B. Shinde, J. Gopalakrishnan and A. K. Tyagi, *Sci. Rep.*, 2016, **6**, 23400.
71 C. J. Howard and H. T. Stokes, *Acta Crystallogr., Sect. B:Struct. Sci.*, 1998, **54**, 782–789.
72 K. Momma and F. Izumi, *J. Appl. Crystallogr.*, 2011, **44**, 1272–1276.
73 Z. Zhang, K. Yuan, J. Zhu, X. Fan, J. Zhou and D. Tang, *Appl. Phys. Lett.*, 2022, **120**, 262201.
74 B. Himmetoglu, A. Janotti, H. Peelaers, A. Alkauskas and C. G. Van de Walle, *Phys. Rev. B: Condens. Matter Mater. Phys.*, 2014, **90**, 241204.
75 N. M. Tubman, C. J. N. Coveney, C.-E. Hsu, A. Montoya-Castillo, M. R. Filip, J. B. Neaton, Z. Li, V. Vlcek and A. M. Alvertis, Phonon-mediated electron attraction in $SrTiO_3$ via the generalized Fröhlich and deformation potential mechanisms, *arXiv*, 2025, preprint, arXiv:2501.17230, DOI: **10.48550/arXiv.2501.17230**.
76 J.-J. Zhou, O. Hellman and M. Bernardi, *Phys. Rev. Lett.*, 2018, **121**, 226603.
77 J. S. Bechtel and A. Van der Ven, *Phys. Rev. Mater.*, 2018, **2**, 025401.
78 K. Guo, T. Weng, Y. Jiang, Y. Zhu, H. Li, S. Yuan, J. Yang, J. Zhang, J. Luo, Y. Grin and J.-T. Zhao, *Mater. Today Phys.*, 2021, **21**, 100480.
79 A. Khan, J. Flitcroft and J. Skelton, *Phys. Chem. Chem. Phys.*, 2024, **27**, 3230–3242.
80 M. Zhang, I. Pallikara, J. M. Flitcroft and J. M. Skelton, *J. Mater. Chem. A*, 2025, **13**, 5415–5426.
81 M. Cardona, *Phys. Rev.*, 1965, **140**, A651–A655.
82 K. van Benthem, C. Elsässer and R. H. French, *J. Appl. Phys.*, 2001, **90**, 6156–6164.
83 M. Kar, *Electronic and optical properties of SrTiO3 perovskite using semi-local and hybrid first principles density functional theory*, 2021.
84 Y. Zhu, J. M. Skelton, D. J. Lewis and R. Freer, *JPhys: Energy*, 2024, **6**, 025027.
85 X.-L. Shi, H. Wu, Q. Liu, W. Zhou, S. Lu, Z. Shao, M. Dargusch and Z.-G. Chen, *Nano Energy*, 2020, **78**, 105195.
86 J. Ravichandran, W. Siemons, D.-W. Oh, J. T. Kardel, A. Chari, H. Heijmerikx, M. L. Scullin, A. Majumdar, R. Ramesh and D. G. Cahill, *Phys. Rev. B: Condens. Matter Mater. Phys.*, 2010, **82**, 165126.
87 J. Wang, B.-Y. Zhang, H.-J. Kang, Y. Li, X. Yaer, J.-F. Li, Q. Tan, S. Zhang, G.-H. Fan, C.-Y. Liu, L. Miao, D. Nan, T.-M. Wang and L.-D. Zhao, *Nano Energy*, 2017, **35**, 387–395.
88 S. Ohta, T. Nomura, H. Ohta, M. Hirano, H. Hosono and K. Koumoto, *Appl. Phys. Lett.*, 2005, **87**, 092108.
89 Z. M. Gibbs, F. Ricci, G. Li, H. Zhu, K. Persson, G. Ceder, G. Hautier, A. Jain and G. J. Snyder, *npj Comput. Mater.*, 2017, **3**, 8.
90 H. Frölich, *Adv. Phys.*, 1954, **3**, 325–361.
91 C. Verdi and F. Giustino, *Phys. Rev. Lett.*, 2015, **115**, 176401.
92 S. LeBlanc, S. K. Yee, M. L. Scullin, C. Dames and K. E. Goodson, *Renewable Sustainable Energy Rev.*, 2014, **32**, 313–327.
93 A. Kikuchi, N. Okinaka and T. Akiyama, *Scr. Mater.*, 2010, **63**, 407–410.
94 H. Wang, C. Wang, W. Su, J. Liu, Y. Zhao, H. Peng, J. Zhang, M. Zhao, J. Li, N. Yin and L. Mei, *Mater. Res. Bull.*, 2010, **45**, 809–812.
95 D. Srivastava, C. Norman, F. Azough, M. C. Schäfer, E. Guilmeau, D. Kepaptsoglou, Q. M. Ramasse, G. Nicotra and R. Freer, *Phys. Chem. Chem. Phys.*, 2016, **18**, 26475–26486.